A noncatalytic activity of the H4K20 demethylase DPY-21 regulates condensin DC binding

Laura Breimann[1,2,3] [*&], Ana Karina Morao[1] [*], Jun Kim[1], David Sebastian Jimenez[1], Nina Maryn[1], Krishna Bikkasani[1], Michael J Carrozza[1], Sarah E Albritton[1], Maxwell Kramer[1], Lena Annika Street[1], Kustrim Cerimi[2], Vic-Fabienne Schumann[2], Ella Bahry[2], Stephan Preibisch[2,4], Andrew Woehler[2], Sevinç Ercan[1&]

[1]Department of Biology, Center for Genomics and Systems Biology, New York University, New York, NY, USA

[2]Berlin Institute for Medical Systems Biology, Max Delbrück Center for Molecular Medicine, Berlin, Germany

[3]Institute for Biology, Humboldt University of Berlin, Berlin, Germany
[4]Janelia Research Campus, Howard Hughes Medical Institute, Ashburn, VA, USA

[*]equal contribution

[&]co-corresponding

keywords: condensin, chromatin, transcription, histone modifications, FRAP, X chromosome, Hi-C, genome organization, TADs, C elegans

ABSTRACT

Condensin is a multi-subunit SMC complex that binds to and compacts chromosomes. Unlike cohesin, *in vivo* regulators of condensin binding dynamics remain unclear. Here we addressed this question using *C. elegans* condensin DC, which specifically binds to and represses transcription of both X chromosomes in hermaphrodites for dosage compensation. Mutants of several chromatin modifiers that regulate H4K20me and H4K16ac cause varying degrees of X chromosome derepression. We used fluorescence recovery after photobleaching (FRAP) to analyze how these modifiers regulate condensin DC binding dynamics *in vivo*. We established FRAP using the SMC4 homolog DPY-27 and showed that a well-characterized ATPase mutation abolishes its binding. The greatest effect on condensin DC dynamics was in a null mutant of the H4K20me2 demethylase DPY-21, where the mobile fraction of the complex reduced from ~30% to 10%. In contrast, a catalytic mutant of *dpy-21* did not regulate condensin DC mobility. Separation of catalytic and non-catalytic activity is also supported by Hi-C data in the *dpy-21* null mutant. Together, our results indicate that DPY-21 has a non-catalytic role in regulating the dynamics of condensin DC binding, which is important for transcription repression.

INTRODUCTION

The evolutionarily conserved structural maintenance of chromosomes (SMC) complexes use the energy from ATP hydrolysis to regulate chromosome structure in various nuclear processes [1]. Condensin is an SMC complex that regulates DNA compaction for chromosome segregation during cell division and genome organization for transcription regulation during interphase [2]. The current model for how condensins compact DNA is through a process called loop extrusion [3,4]. Unlike a related SMC complex called cohesin, the proteins and chromatin factors that regulate condensin binding and loop extrusion processivity are less clear [5]. Here we addressed this question using the *Caenorhabditis elegans* dosage compensation system, where an X-specific condensin binding and function is better understood and serves as a model for the metazoan condensins [6].

In *C. elegans*, X chromosome dosage compensation is mediated by a specialized condensin that forms the core of the dosage compensation complex (DCC) [7]. This X-specific condensin (hereafter condensin DC) is distinguished from the canonical condensin I by a single SMC-4 variant called DPY-27 [8]. The current model of condensin DC binding to the X chromosomes posits that SDC-2, along with SDC-3 and DPY-30, recruit the complex to a small number of recruitment elements on the X *(rex)* [9–11]. From there, the complex spreads linearly along chromatin, accumulating at active promoters, enhancers, and other accessible regulatory sites [12,13]. Condensin DC recruitment and spreading regulate the compaction of the 3D structure of the X chromosomes [14–18].

Condensin DC physically interacts with DPY-21 [19], a Jumanji domain-containing histone demethylase that converts H4K20me2 to H4K20me1 [20], resulting in increased H4K20me1 on the X chromosome [21,22]. This increase leads to deacetylation of H4K16 mediated by SIR-2.1 [22]. As a result, the two dosage compensated X chromosomes in hermaphrodites contain higher H4K20me1 and lower H4K16ac levels. Further analysis indicated that condensin DC and *dpy-21* are also required for lower levels of H3K27ac on the X chromosome [13]. An increase of H4K20me1 and decreased acetylation mirror the histone modification changes on metazoan mitotic chromatin [23], providing a link between canonical condensin and condensin DC binding to chromatin.

In this study, we analyzed the effect of several mutants that regulate H4K20 methylation and H4K16 acetylation on the dynamics of condensin DC binding using fluorescence recovery after photobleaching (FRAP). We established FRAP in *C. elegans* intestine cells using a GFP-tagged DPY-27 and validated the system by demonstrating that condensin DC mobility increases upon depletion of its recruiter SDC-2. We found that introducing a well-characterized mutation in the ATPase domain of DPY-27 eliminated its binding to the X chromosomes as measured by FRAP and ChIP-seq. Mutants that regulate H4K20me and H4K16ac showed subtle effects on condensin DC binding dynamics as measured by FRAP. The most substantial effect was in the *dpy-21* null mutant, which reduced the fraction of mobile DPY-27 from ~30% to ~10%. Unlike

the null mutant, the *dpy-21 JmjC* catalytic mutant did not affect condensin DC mobility, suggesting that DPY-21 role in regulating condensin DC binding dynamics is largely non-catalytic. *Dpy-21(JmjC)* mutant was shown to reduce long-range 3D contacts, including those between the *rex* sites [20]. Intriguingly, *dpy-21* null mutation largely rescued these effects. Together, our results suggest that DPY-21 has a noncatalytic role in regulating the dynamics of condensin DC binding to the X chromosomes, which is important for its function in transcription repression.

MATERIALS AND METHODS

Strains and Worm Growth

A list of strains, genotypes, primer sequences, and sgRNA target sequences are provided in Supplemental File 1. Unless noted, worms were grown and maintained using standard methods at 20-22°C on NGM plates containing OP50-1 strain of *E. coli* as food.

Generation of DPY-27::GFP and DPY-27(EQ)::GFP strains: An inducible GFP-tagged copy of DPY-27 was expressed from the chrII MosSCI site (~8.4 Mb) [24] under the control of a heat-shock inducible *hsp 16-41* promoter and the *dpy-27* 3' UTR. The *Hsp 16-41* promoter was amplified from pCM1.57 using primers SE123 F&R, and *dpy-27* 3'UTR was amplified from genomic DNA using primers SE124F&R and were inserted into pCFJ151 at the XhoI site. The resulting plasmid contained a SphI site between the promoter and the 3' UTR, which was used for NEB Infusion cloning with the full-length *dpy-27* and a GFP-3xflag sequence. Amplification of the *dpy-27* sequence was done from genomic DNA using primers SE135F&R. GFP-3x flag sequence was amplified from a plasmid kindly provided by Susan Strome, using primers SE136 F&R. ATPase mutagenesis of DPY-27 was performed by incorporating the E to Q mutation at the conserved ATPase domain as shown in Figure 2A.

Generation of Halo::DPY-27 strain: The CRISPR/Cas9 system was used to insert the Halo tag at the C-terminus of DPY-27 [25]. A 20 bp crRNA (LS37) was designed to target the end of the last *dpy-27* exon. The dsDNA donors consisting of a 15 bp flexible linker (GlyGlyGlyGlySer) and

the Halo tag flanked by 35 bp homology arms were generated by PCR using 5' SP9 (TEG) modified primers AM29F&R and pLS19 as a template. The injection mix containing *S.pyogenes* Cas9 3NLS (10 μg/μl, IDT), crRNA (2 nmol, IDT), tracrRNA (5 nmol, IDT), dsDNA donors, and pCFJ90 (pharynx mCherry marker). ~40 F1s that were positive for the co-injection marker were transferred to individual plates and allowed to have progeny. F2 progeny was screened by PCR with primers LS40F&R. Sanger sequencing of positive PCR products showed in-frame insertion of the Halo tag along with 18 bp of unknown sequence that did not affect the function of the tagged protein.

Generation of X;V, set-4(n4600) and X;V,dpy21(y607 JmjC) strains: ERC57 (*set-4 (n4600) II; X;V (ypT47)*) strain was generated by crossing YPT47 with the set-4 null deletion mutant strain MT14911. For X;V, *dpy21(*same as *y607 JmjC)* strain, a single amino acid substitution (H1452A), that disrupts the demethylase activity of *dpy-21* [20], was incorporated in the *X;V (ypT47)* strain using CRISPR/Cas9. A 200 bp single-stranded oligonucleotide repair template (BR16_oligo) was used to change the codon 1452 from CAC to GCC. Introduction of the changed codon generated a NotI restriction site that was used to screen and confirmed by Sanger sequencing. BR17F&R primers amplify a 514 bp region that encompasses the mutation site, and NotI digestion generates two fragments of 216 bp and 298 bp only in the mutated allele.

Genomic Data Access

The new genomic data is available at Gene Expression Omnibus (GEO) series numbers GSE169458, and individual accession numbers of the new and published data sets used in this study are listed in Supplemental File 1.

ChIP-seq

For the ChIP-seq analyses of GFP tagged DPY-27 in embryos, gravid adults were heat-shocked at 35°C for 30 min and transferred to room temperature for two hours for recovery. Embryos were collected by bleaching, and ChIP was performed as described previously [26]. Two micrograms of anti-GFP (Abcam ab290) and anti-DPY-26 antibodies were used with 1-2 mg of

embryo extract. Detailed antibody information is given in Supplemental Table 1. The ChIP-seq analysis of the X;V fusion strains was performed in early L3 larvae by hatching embryos in M9 overnight. The next day, L1s were plated on NGM media containing HB101 bacteria and incubated at 20°C for ~24 hours. ChIP in larvae was performed by grinding frozen larvae a few minutes in mortar and pestle cooled in liquid nitrogen, followed by crosslinking in PBS containing 1% formaldehyde for 10 min, quenching with 125 mM glycine for 5 min, and preparing ChIP extract as in embryos. X;V wt rep2 was prepared by live crosslinking larvae. Two micrograms of anti-DPY-27 were used with 1-2 mg of extract per ChIP. Half of the ChIP DNA and approximately 20-80 ng of the input control DNA were used to make Illumina TruSeq libraries as previously described [11]. For each data set, at least two biological replicates were generated as listed in Supplemental File 1. Single-end sequencing was performed in Illumina HiSeq500 or NextSeq.

ChIP-seq data analysis: We used bowtie2 version 2.3.2 to align 50-75 bp single-end reads to WS220 with default parameters [27]. Bam sorting and indexing was performed using samtools version 2.1.1 [28]. BamCompare tool in Deeptools version 3.3.1 was used to normalize for the sequencing depth using CPM and create ChIP/Input ratios with a bin size of 10 bp and 200 bp read extension [29]. Only reads with a minimum mapping quality of 20 were used, and mitochondrial DNA, PCR duplicates, and blacklisted regions were removed [30]. The average coverage data was generated by averaging ChIP-Input enrichment scores per 10 bp bins across the genome. For alignments and sliding window analysis of replicates, ChIP/Input ratios were z-scored using the standard deviation and mean of autosomes or chromosomes I to IV in normal and X;V karyotypes, respectively.

mRNA-seq

mRNA-seq analysis of *sir-2.1* null mutant strain VC199 (*sir-2.1*) was performed as described and compared to previously published mRNA-seq data [31]. Briefly, embryos and L2/L3 larvae were collected for at least three biological replicates. After collection, worms were stored in

Trizol (Invitrogen). RNA was purified using the manufacturer's protocol after freeze-cracking samples five times. RNA was cleaned up using Qiagen RNeasy kit, and mRNA was purified using Sera-Mag Oligo (dT) beads (Thermo Scientific) from 1 μg of total RNA. Stranded Illumina libraries were prepared as described [31], and sequencing was done with Illumina HiSeq-2000 to produce single-end 50-75 bp reads. We aligned reads to the WS220 genome version using Tophat version 2.1.1 with default parameters [32]. Count data was calculated using HTSeq version 0.6.1 [33] and normalized using the R package DESeq2 [34].

Hi-C

CB428 (*dpy-21(e428))* gravid adults were bleached to isolate embryos, which were crosslinked in 50 mL M9 containing 2% formaldehyde, washed with M9 and PBS, and pelleted at 2000 g 1 min to store at -80°C. Approximately 50 μl of the embryo pellet was resuspended and crosslinked a second time using the same conditions, washed once with 50 mL 100mM Tris-Cl pH 7.5 and twice with 50 mL M9. The embryo pellet was resuspended in 1 ml embryo buffer (110 mM NaCl, 40 mM KCl, 2 mM CaCl2, 2 mM MgCl2, 25 mM HEPES-KOH pH 7.5) containing 1 unit chitinase (Sigma) and digested approximately 15 minutes. Blastomeres were then washed with embryo buffer twice by spinning at 1000g 5 min. The pellet was resuspended in 1 mL Nuclei Buffer A (15 mM Tris–HCl pH 7.5, 2 mM MgCl2, 0.34 M Sucrose, 0.15 mM Spermine, 0.5 mM Spermidine, 1 mM DTT, 0.5 mM PMSF, 1xCalbiochem Protease Inhibitor cocktail I, 0.25% NP-40, 0.1% Triton X-100), centrifuged at 1000 g for 5 minutes at 4°C then resuspended in 1.5 mL Nuclei Buffer A. The embryos were dounced ten times with a loose pestle A and ten times with a tight pestle B. The cellular debris was spun down 1 min at 200 g. The supernatant containing nuclei was kept on ice. The pellet was resuspended in 1.5 mL Nuclei Buffer A, and the douncing process was repeated four times. Each supernatant was checked for absence of debris by DAPI stain and pooled and spun down at 1000 g for 10 mins at 4°C. Approximately ~20 μl of nuclei were used to proceed to the Arima Hi-C kit, which uses two 4-base cutters, DpnII (^GATC) and HinfI (G^ANTC), followed by KAPA Hyper Prep Kit for library preparation per the protocol provided by Arima. Paired-end Illumina sequencing was performed with Nextseq or Novaseq.

Hi-C data analysis: 150bp reads were trimmed using fastx toolkit version 0.0.14 to match replicates generated by 100-bp paired-end sequencing. The Hi-C data was mapped to ce10 (WS220) reference genome using default parameters of the Juicer pipeline version 1.5.7 [35]. Because Hi-C data generated from the Arima Hi-C kit used two restriction enzymes, dpnII (^GATC) and hinfI (G^ANTC), while the published Hi-C data used only one, dpnII (^GATC), the corresponding restriction sites files were used for the juicer pipeline. The mapping statistics from the inter_30.txt output file are provided in Supplemental File 1. The inter_30.hic outputs were converted to h5 using the hicConvertFormat of HiCExplorer version=3.5.1 for genome-wide normalization and sample-to-sample depth normalization. [36–38]. The inter_30.hic files were first converted to cool files, and the correction method was removed using the --correction_name none option. Then, cool files were converted to h5 files to be used in HiCExplorer. The replicates of the same experimental condition were combined using hicSumMatrices. The count values of each replicate were normalized to match those of the most shallow matrix using hicNormalize with the option --smallest. The same method was used for the summed matrices. Lastly, the hicCorrectMatrix function was applied to each matrix to correct for sequencing bias with the following parameters: --correction_method ICE, -t 1.7 5, --skipDiagonal, --chromosomes I II III IV V X. The distance decay curves were generated by computing the average contact for a given distance using the 5000 bp-binned normalized matrix using hicPlotDistVsCounts with parameters --perchr, maxdepth 20,000,000. The outputs from --outFileData were plotted in R. The curves were normalized to unity to compare different samples by setting the sum of contacts in the distance range of 5000 bp to 4 Mb range to 1 for each chromosome. To analyze X-specific changes, we calculated P(s,chrX)/P(s,chrA) by dividing the P(s) of the X chromosome by the average P(s) of all autosomes at every distance, s. The insulation scores were computed using the 10kb-binned normalized matrix with the function hicFindTADs using parameters: --correctForMultipleTesting fdr, --minDepth 80000, --maxDepth 200000, --step 40000. The meta-loops were computed using the 10 kb-binned normalized matrix with the hicAggregateContacts function of hicexplorer with parameters: --range 100000:3000000, --avgType mean, --transform obs/exp, --plotType 3d, --vMin 0.8 --vMax 2

--BED 17 strong *rex*es [11]. A 400 bp window for the 17 strong rex sites defined in was used as center regions with an additional 250 kb up and downstream regions.

Immunoprecipitation and Western blots

Immunoprecipitations (IPs) of GFP tagged DPY-27 proteins were performed from protein extracts prepared using 200 μL of young adult worms heat-shocked at 35°C for one hour and let to recover at 20°C for the indicated times. For IPs from embryos, heat-shocked adults were bleached after recovery to obtain ~100 μl embryos. Worms were dounced in lysis buffer (40 mM HEPES pH 7.5, 10% glycerol, 150 mM NaCl, 1 mM EDTA, and 0.5% NP-40) complemented with protease inhibitors (Calbiochem cocktail I) and sonicated for 5 min (30 sec on and 30 sec off in a Bioruptor). Extracts were centrifuged at 17,000 g for 15 min at 4°C, and 2 mg of protein were incubated overnight with 2-3 μg of the indicated antibody. Immunocomplexes were collected with protein A Sepharose beads at 4°C for 2 hours. Beads were washed thrice with 1 ml of immunoprecipitation buffer (50 mM HEPES-KOH pH 7.6, 1 mM EDTA, 0.05% Igepal, and 150 mM NaCl). IPed proteins were eluted by boiling in SDS sample buffer and analyzed by SDS-PAGE and immunoblotting using an anti-DPY-27 antibody (1:2000). Detection was performed using ECL Plus reagents (#PI80196, ThermoFisher).

Worm size analysis

Quantification of the worm size was performed in the young adult stage. Worms were allowed to lay eggs for 4 hours, and the progeny was grown at 20°C to a young adult stage. Worms were washed with M9, anesthetized with 10 mM levamisole, and placed on a fresh NGM plate without OP50 to achieve an even and clear background. Worms were singled with an eyelash, and images of about 30 worms were acquired using a Dino-Lite eyepiece camera (AM7025X) on a Zeiss stereomicroscope with a 1X magnification. For analysis, the background was subtracted using Fiji [39] with a rolling ball radius of 50 px (light background). To analyze the worms' size and width, the Fiji plugin WormSizer [40] was used and plots were created using Python (https://github.com/ercanlab/2021_Breimann_et_al)

Heat shock, fluorescent labeling, and mounting worms for imaging

JF549-HaloTag and JF635-HaloTag ligands were a generous gift from Luke D. Lavis and Jonathan B Grimm [41,42] and were incorporated into worms by feeding based on [43] with the following modifications. L4 worms were washed and collected in small eppendorf tubes with 200 µl M9, concentrated OP50, and 2.5 µM HaloTag dye. Tubes rotated at RT for about 17 hours, and worms were then placed on fresh OP50 plates for at least 4 hours to reduce the background signal of the unbound HaloTag ligand.

For imaging experiments using the heat shock inducible DPY-27::GFP, worms were grown to young adult stage and heat-shocked for 1 hr at 35°C, recovered at RT for 8 hr (unless otherwise labeled). Worms were settled in M9 at 4°C for 10 min, and 40 µl were transferred to a well depression microscopy slide with the addition of 10 µl of 50 mM levamisole (LGC). After 10 minutes, the worms were transferred onto a 10% agarose pad on a microscope slide and covered with a 1.7 µm objective slide (high precision, no.1.5H, Marienfeld). Excess liquid was removed using a lab tissue (Kimtech precision wipe), and the edges of the objective slide were sealed with a two-component silicone glue (picodent twinsil speed).

Confocal microscopy and FRAP

Confocal imaging and FRAP were performed on a scanning confocal microscope (Leica SP8) using an HC PL APO 63x 1.3 NA glycerol objective (Leica) and Leica Application Suite X (version 3.5.5.19976). For wGFP, the white light laser was set to 482 nm with 10-15% laser intensity, and the emission detection was set to 488 - 520 nm with a HyD hybrid photodetector and gain of 162%. For JF549, the white light laser was set to 549 nm with 10% laser intensity, and the emission detection was set to 554-651 nm with a HyD detector and gain of 200% and gating between 0.3 - 6.0. For JF635, the white light laser was set to 633 nm with 10% laser intensity, and the emission detection was set to 638-777 nm with a HyD detector and gain of 100% and gating between 0.30 - 6.00.

For FRAP in the intestine nuclei, 20 pre bleach images were acquired, followed by a point bleach (smallest possible bleach spot) of 700 ms with 100 % laser power and subsequent acquisition of ~500 recovery images using 10-15% laser power. The scan speed was set to 600 Hz, with bidirectional scanning (phaseX: 29.752) in a frame size of 256 x 256 pixels (Pixel dwell time 0,002425 s). The pinhole was set to 1 AU, and a 7x digital zoom was used to zoom in to single intestine nuclei of young adult worms. The FRAP experimental protocol can be found here: https://dx.doi.org/10.17504/protocols.io.bpkymkxw

FRAP data analysis

Image analysis of the fluorescence recovery at the bleach point was performed using a custom-written script in MATLAB (MathWorks). First, lateral drift in pre- and post-bleach image stacks was corrected using DFT-based sub-pixel image registration [44]. The area of each intestine nucleus was then manually segmented. The bleached region was determined by automated thresholding (Otsu's Method) of an image of the difference of the mean pre-bleach images and the mean of the first five post-bleach images. Acquisition bleaching was detected in the mean intensity of the whole nucleus region of interest in the post-bleach images. This decrease in intensity was fitted with a monoexponential decay and used to correct the acquisition bleaching during fluorescence recovery. To correct for differences in initial intensity and extent of photobleaching, such that different datasets could be directly compared, each acquisition bleaching corrected curve was then normalized to an initial value of 1 and an immediate post-bleach value of 0. To estimate the fraction of fluorescent proteins that can diffuse into the bleached region during the experiment's time course (mobile fraction) and the recovery time constant (τ), the post bleach recovery was fitted with monoexponential function with nonlinear least-squares-based fitting. The recovery half-time (t1/2), corresponding to the time required to recover half of the fluorescence maximum, is estimated directly from the data. The mean normalized relative intensity of all repeats for each experimental condition was calculated and plotted for each time point with the standard error of the mean using Python. The MATLAB analysis script can be found here: https://github.com/ercanlab/2021_Breimann_et_al

Intensity distribution analysis

To compare the protein expression and X-enrichment of DPY-27::GFP and DPY-27(EQ)::GFP images were recorded at 3 and 8 hours after a 1-hour heat-shock at 35°C. 2D images were manually segmented for the nuclear region, and pixel intensity values for the GFP tagged proteins were recorded for at least 20 images per condition. To compare the average density of pixel intensities per condition, the pixel intensities were binned to ranges of 20, summed for all images of one condition, and divided by the number of used images using Python.

To compare image intensities of endogenous DPY-27::Halo in wild-type and *dpy-21 null* conditions, worms were stained with HaloTag-JF549, as described above, and z-stack images were recorded to capture the complete intestinal nuclei. To compare DPY-27::Halo enrichment at the X chromosome between different conditions, the HaloTag signal was segmented in 3D using autocontex pixel classification in ilastik, resulting in a simple segmentation that assigns the most probable class for each pixel [45]. Using Fiji [39], a binary 3D mask was created from the ilastik segmentation using Otsu's method and used to segment the HaloTag signal. Binned pixel intensities were recorded from both conditions, and density plots were created using Python https://github.com/ercanlab/2021_Breimann_et_al.

Recombinant protein and peptide binding assay

The DNA encoding for amino acids 351-661 of the DPY-28 protein was amplified from cDNA using the primers DPY 28 351F & DPY-28 660R (Supplemental File 1- Primers). The cDNA template was prepared from total RNA using SuperScript III (Invitrogen) according to the manufacturer's protocol. The PCR product was digested with BamHI and EcoRI and cloned into corresponding sites in pGEX-5X-2. The plasmid was transformed to a BL21 codon + *E. coli* strain to be induced with 1 mM IPTG for 3 hours at 25°C and purified using standard GST protein purification using GE Healthcare Glutathione Sepharose 4B based on the manufacturer's protocol, and the protein amount was quantified using a Bradford assay. The peptides were kindly provided by Brian Strahl (Supplemental Figure 3D). Briefly, 60 μl of the magnetic streptavidin beads (Dynabeads M280; Invitrogen) were washed twice with 1 ml recombinant protein binding buffer (rPBB) (50 mM Tris pH 8, 0.3 M NaCl, 0.1% Igepal CA360) and

incubated rotating 1 hour with 1 nmol peptide at 4°C. The beads were washed twice with rPBB and incubated with 40 pmol of recombinant protein for 3 hours, rotating at 4°C. The beads were washed 5 min thrice with rPBB and resuspended in 30 µl SDS sample buffer, and 15 µl was run on a 4-12% Bis-Tris MOPS gel (Invitrogen) transferred to a PVDF membrane and was blocked with 1XPBST (0.1%Tween-20) containing 5% dry milk. Bound peptides were visualized using an anti-GST antibody (GE 27-4577-50) 1:2,000, Anti-goat-HRP (Promega V8051) 1:10,000 ECL-Plus (GE), and the Typhoon Scanner.

RESULTS

FRAP measurement of condensin DC binding *in vivo*

To analyze condensin DC binding *in vivo*, we used FRAP, which measured functionally relevant dynamics of condensin binding in budding yeast [46] and condensin I and II complexes in human cells [47,48]. We set up the FRAP system using DPY-27, the SMC4 homolog that distinguishes condensin DC from I (Figure 1A). To fluorescently label DPY-27, we added a Halo tag endogenously at the C-terminus using CRISPR/Cas9 genome editing. Unlike *dpy-27* mutants, which are lethal or dumpy, the resulting animals were phenotypically wild-type, indicating that the tagged protein complements protein function. This was also supported by subnuclear localization of DPY-27::Halo, which is typical of X-specific localization of the DCC (Figure 1B) [9,10]. DPY-27::Halo did not photobleach sufficiently in our hands, and endogenous tagging by GFP did not produce a strong signal. Thus, we turned to expressing a GFP-tagged copy of DPY-27 using a heat-inducible promoter to perform FRAP. First, we characterized the expression of the transgene by incubating adults at 35°C for 1 hour then moving them to the normal growth temperature of 20°C. After 3 hours at 20°C, excess DPY-27::GFP was visible across the nuclei, but after 8 hours, localization was constrained to a subnuclear domain suggesting that the remaining protein bound specifically to the X chromosomes (Figure 1C).

We validated that DPY-27::GFP forms a complex and binds to DNA as expected in three ways. First, we analyzed the localization of DPY-27::GFP after 8 hours of recovery in intestine cells in the presence of the Halo-tagged endogenous protein. DPY-27::GFP colocalized with

DPY-27::Halo, indicating proper localization (Figure 1B, Supplemental Figure 1A). Second, DPY-27::GFP immunoprecipitated condensin DC subunits, supporting complex formation (Figure 1D). Third, DPY-27::GFP was enriched on the X chromosomes, and the ChIP-seq binding pattern followed that of DPY-26, the kleisin subunit of condensin DC (Supplemental Figure 1B).

We chose intestine cells for performing FRAP, where the nuclei are large due to polyploidy, and subnuclear localization of the complex is easily detected (Figure 1E). Previous studies also used these cells to analyze condensin DC binding by immunofluorescence [9,19,20,22]. In addition, controlling DPY-27::GFP expression in intestines was easier than in embryos, where nuclei were small (Supplemental Figure 1C) and there was variability in heat-induced expression of DPY-27::GFP (Supplemental Figure 1D).

To further validate the FRAP assay in the intestine cells, we compared DPY-27::GFP recovery to that of free NLS::GFP and histone H2B::GFP (Figure 1E-H). FRAP allows two types of quantitative measurements on protein mobility. First is the proportion of mobile molecules, calculated from the percentage of the recovered signal at the bleached area by replacing bleached molecules. Second is the recovery speed, where a fast recovery indicates diffusion, transient binding slows down the recovery, and stable binding increases the immobile fraction [49]. As expected, the mobile fraction of free GFP (Figure 1G) and recovery half-life (Figure 1H) was much faster than that of histone H2B. H2B::GFP minimally recovered during the experiment time frame and was therefore excluded from the half-life recovery plot. This result is in line with FRAP experiments in human cell lines reporting a mobile fraction for most H2B-GFP of 4% with a T-half recovery of over 2 hours [50].

DPY-27::GFP mobile fraction was ~30% and half time of recovery ~2.6 seconds. FRAP results from different experimental set-ups with different imaging settings and analysis strategies can differ significantly [51]. However, the time scale for DPY-27::GFP is similar to recovery half-times reported in *Saccharomyces cerevisiae* for Smc4, ~2 and ~6 seconds in G1 and M

phase respectively [46] and different from residence times reported for human condensin I and II with a range of ~2-10 min [47,48]. Human condensin I binds more dynamically to chromatin than condensin II. During metaphase, condensin I has a residence time of ~3 min with a mobile fraction of 80%. Condensin II, which binds to chromatin throughout the cell cycle, has a residence time of >5 min with a mobile fraction of 40% [47,48]. Our results indicate that DPY-27 has a higher chromosome-bound fraction than human condensin I and II but has comparable recovery half-times to those reported in yeast.
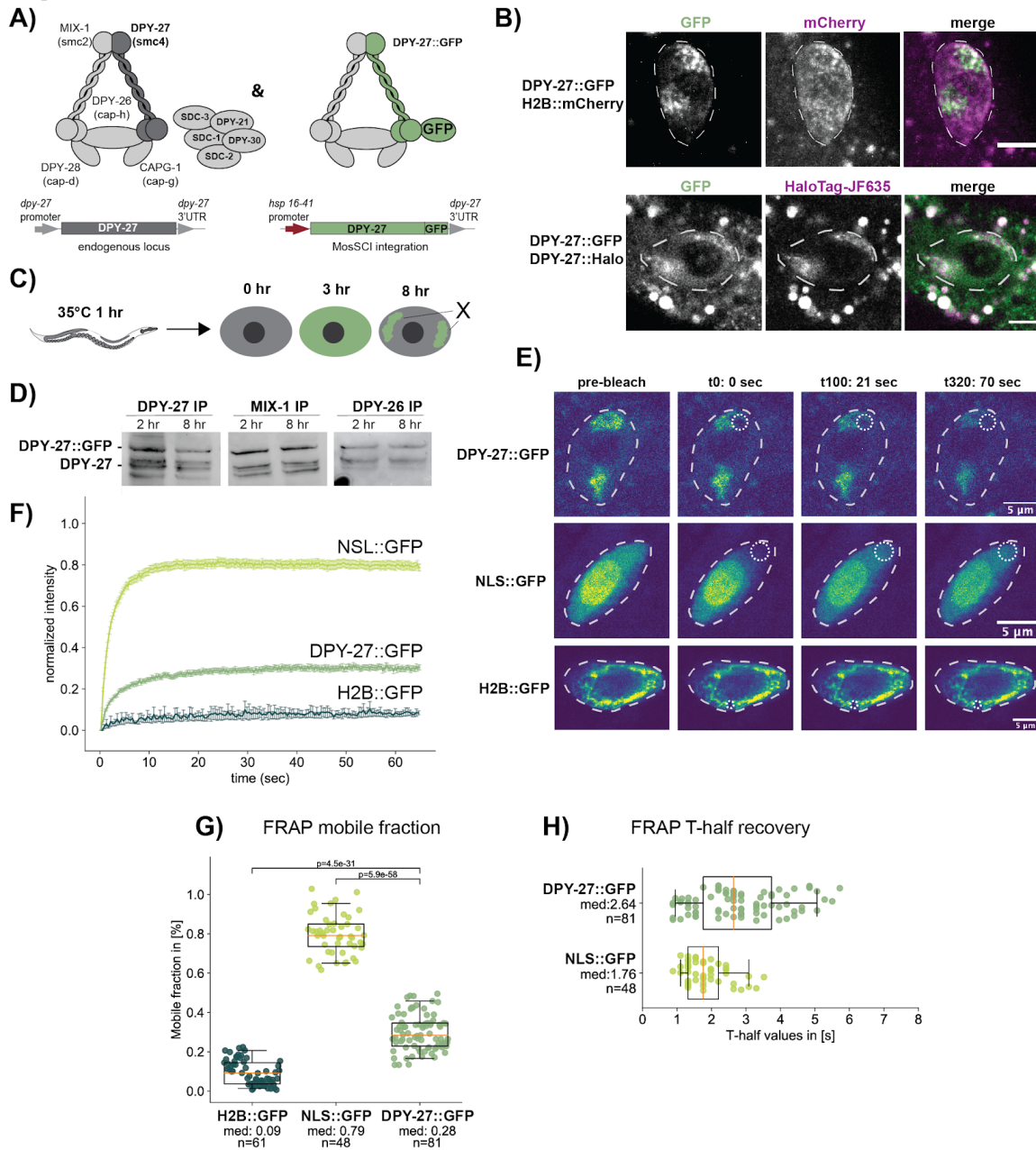
Figure 1) Fluorescence recovery after photobleaching (FRAP) analysis of condensin DC binding

A) Left panel illustrates condensin DC along with the rest of the DCC subunits. The right panel indicates the expression of GFP tagged DPY-27 under the control of a heat-shock inducible promoter at the Chr II MosSCI site.

B) DPY-27::GFP subnuclear localization to the X chromosomes after heat-induced expression (top row) was validated by colocalization with the endogenously tagged DPY-27::Halo stained with JF635 HaloTag ligand (bottom row). The scale bars correspond to 5 μm.

C) Illustration of worms heat shocked for 1 hour at 35°C and fluorescence followed in the large intestinal cells. DPY-27::GFP subnuclear localization is apparent after 8 hours of recovery.

D) DPY-27::GFP binding with condensin DC was validated by co-immunoprecipitation with MIX-1 and DPY-26. Young adult worms were used for IP either 2 or 8 hours after heat shock at 35°C for 1 hour. The ratio of GFP tagged DPY-27 to the endogenous protein in the DPY-27 IP lane indicates the relative abundance of each protein. The ratio in the other lanes indicates the relative interaction of endogenous and DPY-27::GFP with IPed subunit.

E) FRAP sequence for intestine nuclei of adult *C. elegans* worms expressing either DPY-27::GFP, NLS::GFP, or H2B::GFP. The first column of images depicts the first image of the pre bleach series (a total of 20 images). The second column shows the first image after the single point bleach with the bleached area indicated by the small dotted circle. The two following columns depict two time points after the bleach point, t100 (21 seconds) and t320 (70 seconds). The scale bars correspond to 5 μm.

F) Mean FRAP recovery curves from wild-type DPY-27::GFP, H2B::GFP, and NLS::GFP expressing worms. Error bars denote the standard error of the mean (s.e.m.). Number of bleached single intestine nuclei (from at least 3 biological replicates) for each experiment is n = 81 for DPY-27::GFP, n = 48 for NLS::GFP and n= 61 for H2B::GFP.

G) Mobile fractions for the different GFP tagged proteins or free GFP. The mobile fraction is the lowest for H2B::GFP and the highest for NLS::GFP. The mobile fraction for DPY-27::GFP is ~28%. P values are from an independent two-sample t-test.

H) FRAP half-time recovery values for the bleach curves of Figure 1F. The half-time recovery for NLS::GFP shows a shorter diffusion time than DPY-27::GFP. H2B::GFP is
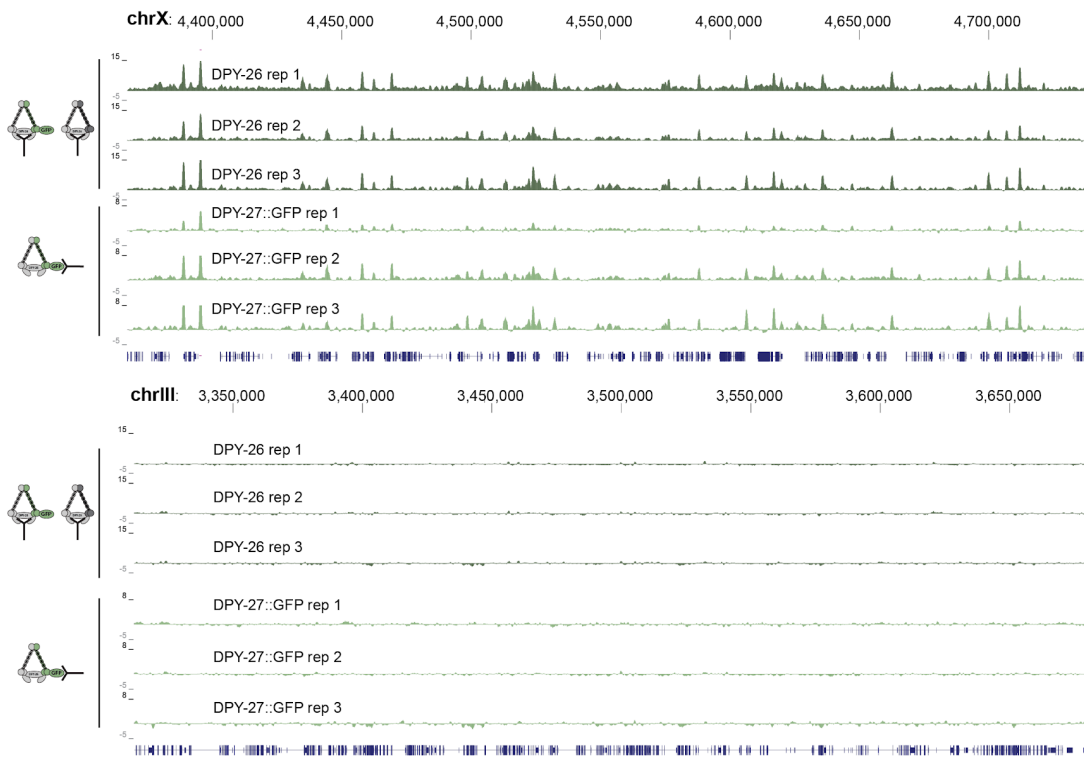
not shown due to the very low recovery of the fluorescence signal during the experimental time frame.
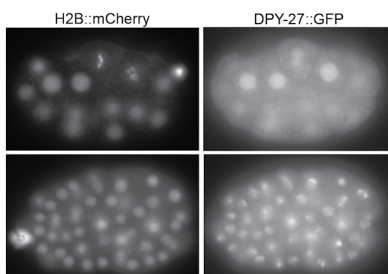
Supplemental figure 1

A)
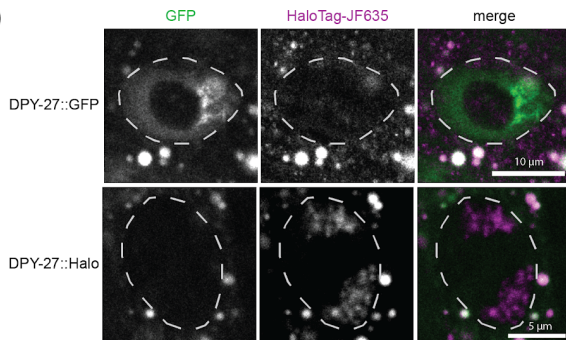
B) ChIP-seq in embryos expressing heat shock inducible DPY-27::GFP
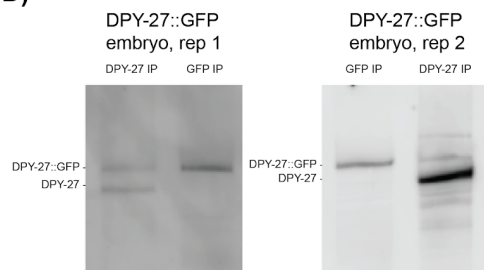

C)

D)

Figure 1) Supplements

A) Validation of separable GFP and JF635-Halo signal. Fluorescent images of intestine nuclei after feeding JF635-Halo ligand in homozygous worms expressing heat-shock inducible DPY-27::GFP (upper row) or endogenously Halo-tagged DPY-27 (lower row). Both worm lines were stained with JF635-Halo ligand and heat-shocked. White dotted lines mark nuclei.

B) Validation of DPY-27::GFP localization specifically to the X chromosomes by ChIP-seq. DPY-27::GFP ChIP-seq analysis replicates using anti-GFP antibody in embryos. DPY-26 ChIP-seq was used as a positive control in the same extracts.

C) X-localization of DPY-27::GFP in embryos is indicated by subnuclear puncta that appears later in embryogenesis when condensin DC localizes specifically to the X chromosomes. H2B::mCherry and DPY-27::GFP signal 6 hours after a heat-shock in early (before X localization and late embryos (after DC localization to the X).

D) Heat shock expression of DPY-27::GFP was variable in embryos. Two examples are shown where immunoprecipitation of DPY-27 showed different proportions of GFP tagged DPY-27 (top band) compared to endogenous (bottom band). Protein extracts were prepared from embryos isolated from gravid adults that were heat-shocked 30 min at 35°C and recovered at room temperature for 2 hours.

ATP hydrolysis is required for condensin DC binding to the X chromosomes

If FRAP measures changes in condensin DC binding dynamics, we reasoned that knockdown of its recruiter SDC-2, and a well-characterized ATP hydrolysis mutation that is known to eliminate the function of other SMC4 homologs, should affect DPY-27 binding dynamics. In condensins, the two heads of SMC2 or SMC4 form the two halves of the ATPase domain; each head interacting with the other in the presence of an ATP molecule, hydrolysis of which dissociates the heads [1]. To test if the ATP hydrolysis by DPY-27 is necessary for its binding to DNA, we inserted a walker B mutation (E to Q, Figure 2A) that nearly eliminates ATP hydrolysis in human [52], *Xenopus* [53], yeast [46,54], and chicken [55]. Unlike wild-type DPY-27::GFP,

DPY-27(EQ)::GFP failed to show subnuclear enrichment indicative of localizing to the X chromosome (Figure 2B). The conclusion that ATP hydrolysis by DPY-27 is required for its localization to the X was further supported by ChIP-seq analysis of DPY-27::GFP and DPY-27(EQ)::GFP in embryos. Unlike wild-type, the ATPase mutant failed to bind to the X chromosomes (Figure 2C, Supplemental Figure 2A).

Next, we asked if the ATPase mutant improperly interacted with chromatin and showed a dominant-negative effect. The mobility of DPY-27(EQ)::GFP was slightly lower than that of unbound DPY-27::GFP generated by knockdown of condensin DC recruiter SDC-2, thus the mutant may incorrectly associate with chromatin (Figure 2D, Supplemental Figure 2B). Supporting a small dominant-negative effect, mRNA-seq analysis of embryos expressing DPY-27(EQ)::GFP showed slightly higher X chromosome derepression than those expressing DPY-27::GFP (Supplemental Figure 2C). It is possible that the induced expression of the ATPase mutant negatively regulates DPY-27 as proposed for SMCL-1, an SMC-like protein with an ATPase hydrolysis mutation similar to the EQ mutation [56].

To test if the failure of DPY-27(EQ)::GFP to bind is due to its inability to form a complex, we performed co-immunoprecipitation experiments (Figure 2F). We noticed that both wild-type and EQ mutant DPY-27::GFP interacted well with MIX-1 (SMC-2 homolog). However, DPY-27::GFP co-IPed better with DPY-26 (kleisin subunit of condensin I and DC) compared to DPY-27(EQ)::GFP, suggesting that ATPase mutation affects SMC-kleisin interaction. Furthermore, unlike wild-type DPY-27, the EQ mutant protein is reduced over time (Figure 2B). Directly after the heat shock, DPY-27 and the EQ mutant proteins are expressed at similar levels. However, after 8 hours, when DPY-27::GFP binding to the X is clearly visible, the ATPase mutant level is strongly decreased. It is possible that ATPase mutant DPY-27, which is unable to complex and/or bind to DNA, is degraded. Nevertheless, a considerable fraction of DPY-27(EQ)::GFP protein was in a complex; thus, the EQ mutant's failure to localize to the X indicates that ATP hydrolysis is required for stable association of condensin DC with the X chromosomes.
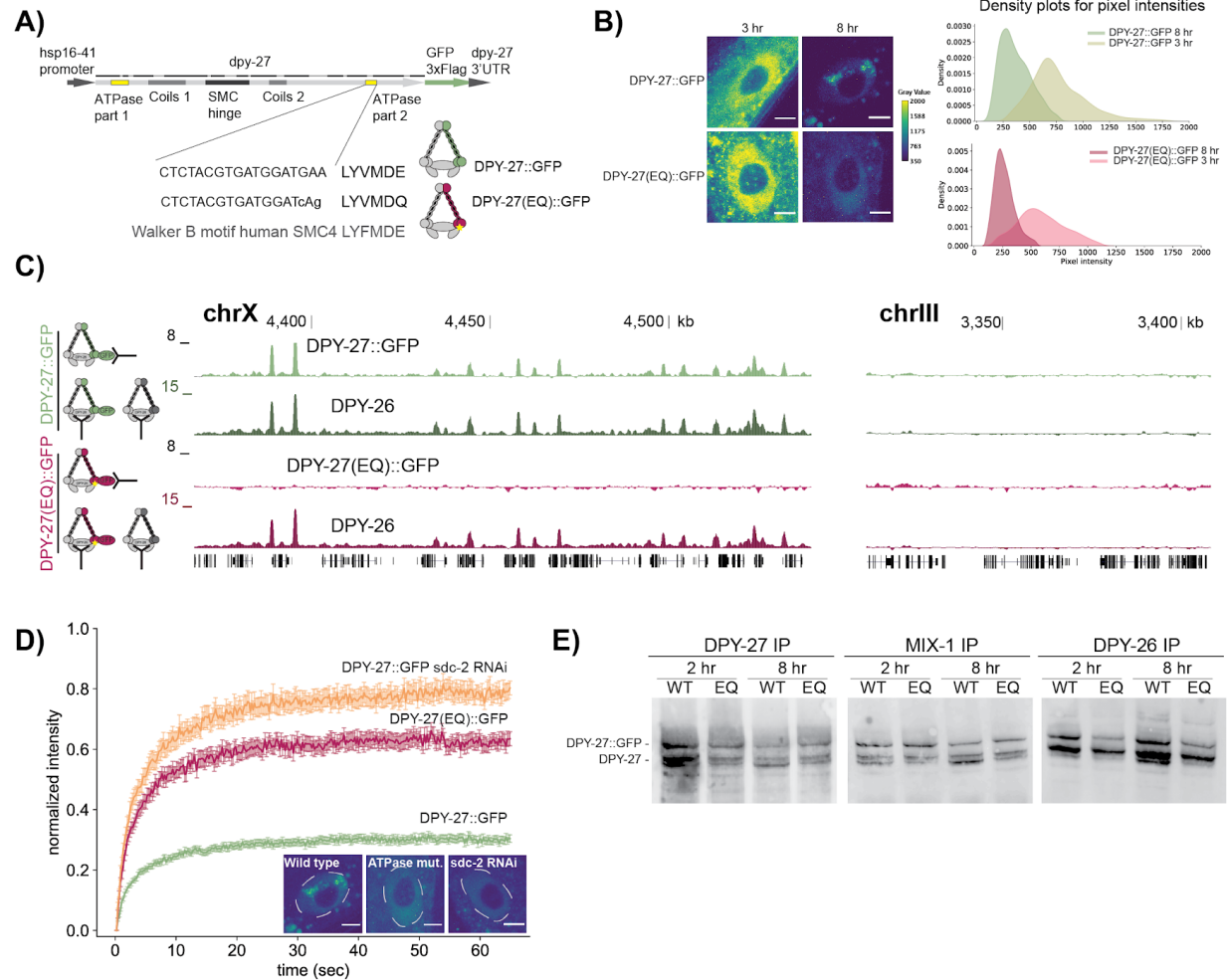
Figure 2) The effect of a conserved SMC ATPase mutation on DPY-27 binding, function, protein stability, and complex formation

A) Heat shock inducible GFP tagged *DPY-27(EQ)*. The DNA sequence coding for the conserved Walker B motif and the E to Q mutation are shown below.

B) Localization of the wild-type and EQ ATPase mutant DPY-27::GFP proteins in intestine cells. Adults were heat-shocked at 35°C for 1 hour and recovered for either 3 or 8 hours. Unlike DPY-27::GFP, ATPase EQ mutant did not show subnuclear localization. Additionally, the ATPase mutant was present only in a very low amount after the 8-hour recovery suggesting degradation of nonfunctional DPY-27. The right panel depicts

quantification of the GFP signal's pixel intensities in the nuclei after 3 and 8 hours of recovery from heat shock. The intensities were recorded from at least three biological replicates in adult intestine cells. For wild-type, DPY-27::GFP 21 images were used for the 3-hour intensity curve and 26 for the 8 hours recovery time point. For the intensity curves of DPY-27(EQ)::GFP, 44 images were used for the short time point and 36 images for the long recovery time point. The scale bar corresponds to 5 μm.

C) ChIP-seq analysis of wild-type and ATPase mutant DPY-27(EQ)::GFP using anti-GFP antibody in embryos. ChIP against DPY-26 was used as a positive control in the same extracts. Unlike the wild-type protein, ATPase mutant failed to bind the X, and both did not localize to the autosomes; a representative region from chromosome III is shown on the right panel.

D) Mean FRAP recovery curves from DPY-27::GFP, DPY-27(EQ)::GFP and DPY-27::GFP upon SDC-2 RNAi. FRAP was performed ~8 hr after the heat shock. Error bars denote s.e.m. Number of bleached single intestine nuclei (from at least 3 biological replicates) for each experiment is n = 81 for DPY-27::GFP, n= 37 for DPY-27(EQ)::GFP and n= 32 for DPY-27::GFP sdc-2 RNAi. The small images depict example pictures of intestine nuclei used for FRAP analysis. Unlike DPY-27::GFP, ATPase EQ mutant did not show subnuclear localization, similar to when condensin DC recruiter SDC-2 was knocked down. Scale bars correspond to 5 μm.

E) Co-immunoprecipitation analysis of condensin DC subunits. Protein extracts were prepared from larvae that were heat-shocked for 1 hour at 35°C and recovered at room temperature for 2 hours or 8 hours. Immunoprecipitated (IP) proteins were blotted by an anti-DPY-27 antibody. The comparison of GFP tagged DPY-27, and the EQ mutant to the endogenous protein indicates the relative interaction of the GFP tagged proteins with the IPed condensin subunit compared to endogenous.
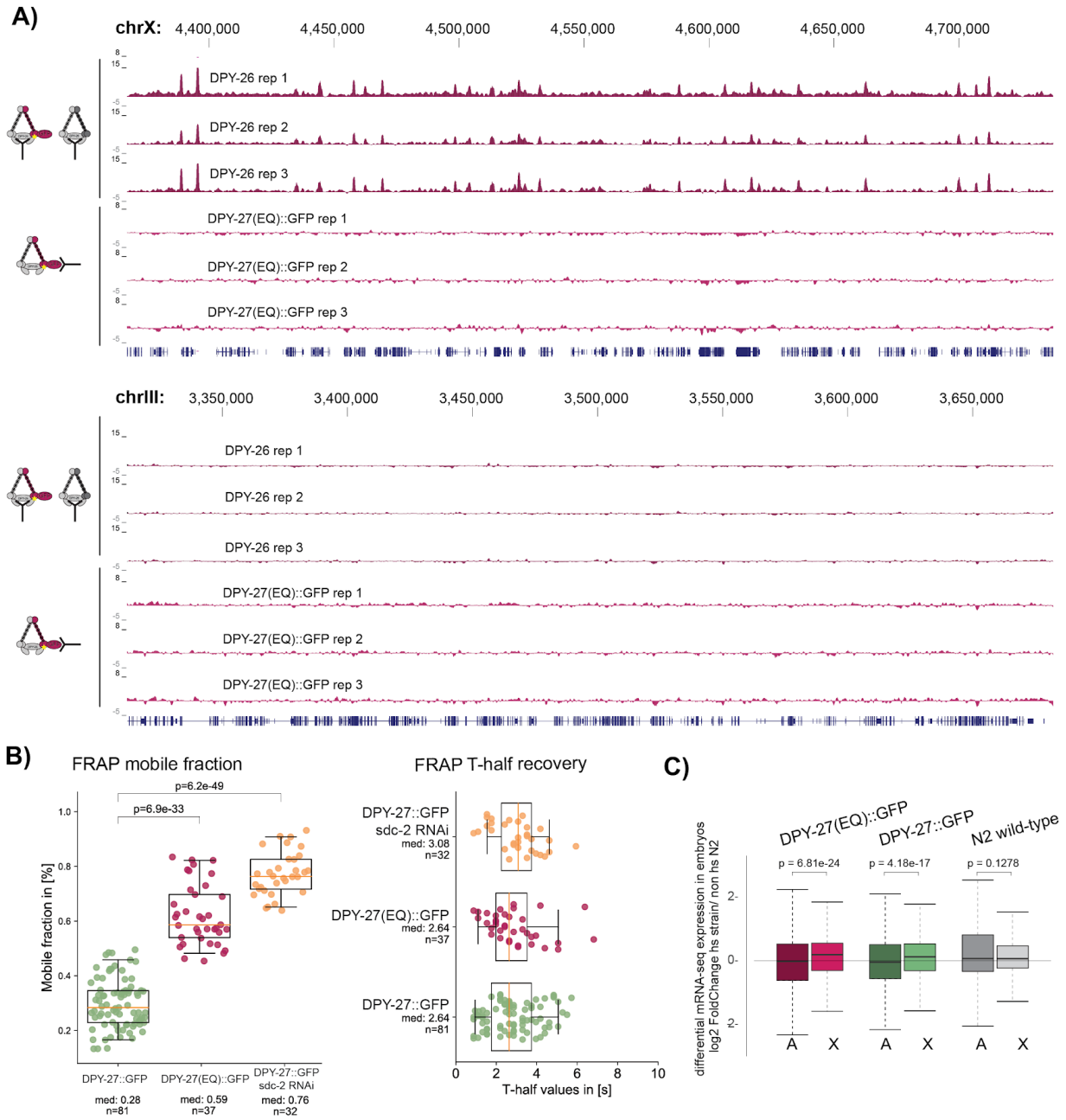
Figure 2) Supplements

A) ChIP-seq data from replicates corresponding to Figure 2C. Replicates for the wild-type DPY-27::GFP ChIP-seq data can be found in Figure S1D.

B) FRAP analysis of mobile fractions (left panel) and T-half recovery time (right panel) corresponding to Figure 2D. P values are from an independent two-sample t-test.

C) Log2 fold changes in mRNA-seq between heat-shocked strains and non-heat-shocked wild-type embryos, collected after 30 min heat shock at 35°C followed by 2-hour recovery. P values are from a Wilcoxon–Mann–Whitney test.

Recombinant DPY-28 HEAT repeat domain bind to histone H3 and H4 peptides in vitro

We wondered if histone modifications on chromatin regulate dynamics of condensin binding and took a candidate approach, considering histone modifiers that were shown to have a role in *C. elegans* dosage compensation, *set-1* H4K20me and *set-4* H4K20me2 transferases, *dpy-21* H4K20me2 demethylase, and *sir-2.1* H4K16 deacetylase [22,31] (Figure 3A). A catalytic mutant of DPY-21, *dpy-21(JmjC)* that nearly eliminated its demethylase activity also showed dosage compensation defects, albeit at a lower level than the null mutant [20]. Similarly, we found that *sir-2.1* null mutant also leads to a slight X derepression (Supplemental Figure 3A) and dumpiness, a phenotype indicating dosage compensation problems (Supplemental Figure 3B).

We first considered how condensin DC might interact with histones (Figure 3B). HEAT repeats, a helical protein structural motif that mediates protein and DNA interactions, are present in the CAPD and CAPG subunits of condensins [57]. Recombinant HEAT repeat domains from condensin II interacted with H4 peptides monomethylated at lysine 20 [58]. We asked if the HEAT repeats in condensin I/DC also interact with histone tails. The HEAT repeats in CAPG-1 are predicted to bind DNA [59]. Thus, we focused on the DPY-28 (CAPD-2 homolog) and identified its HEAT repeat domain using homology to human hCAP-D2 and pfam HEAT predictions (Figure 3C).

We performed an *in vitro* in-solution peptide binding assay using the recombinant protein (Supplemental 3C) and 23 aa N terminal H4 peptides that are unmodified, mono, di, and trimethylated at lysine 20, and unmodified and tetra-acetylated H3 (K4,9,14,18) and H4 (K5,8,12,16) (Supplemental Figure 3D). Recombinant DPY-28 HEAT repeat domain interacted with unmodified 23 aa H4 and 20 aa H3 N-terminal peptides. Tetra-acetylation or increased methylation of lysine 20 reduced the interaction (Figure 3D). Thus, histone modifications have the potential to regulate condensin DC interaction with chromatin.

SET-4, SIR-2.1, and catalytic activity of DPY-21 do not regulate condensin DC binding

While there is a potential for condensin DC interaction with histones, previous studies showed little effect of chromatin modifier mutants on condensin DC localization, except a slight reduction of DPY-27 ChIP-seq signal across promoters in the *dpy-21* null mutant [20–22,31]. We performed DPY-27 ChIP-seq in *sir-2.1* null embryos, and again, did not see a significant difference in condensin DC binding to the X chromosomes compared to wild-type (Figure 3E). To further rule out the effect of chromatin modifiers, we used X;V fusion chromosomes, where the gradual spreading of condensin DC into the autosomal region may be more sensitive for detecting binding changes [12,13]. We were unable to obtain a homozygous X;V fusion in the *dpy-21* null background, thus we analyzed *dpy-21(JmjC)* and *set-4* null mutants (Figure 3F, Supplemental Figure 3F). In both wild-type, *dpy-21(JmjC)* and *set-4* null backgrounds, ChIP-seq replicates showed variable changes in condensin DC spreading into autosome (Figure 3G). Thus, *set-4*, *sir-2.1*, and the catalytic activity of *dpy-21* do not regulate condensin DC binding as measured by ChIP-seq.

Figure 3

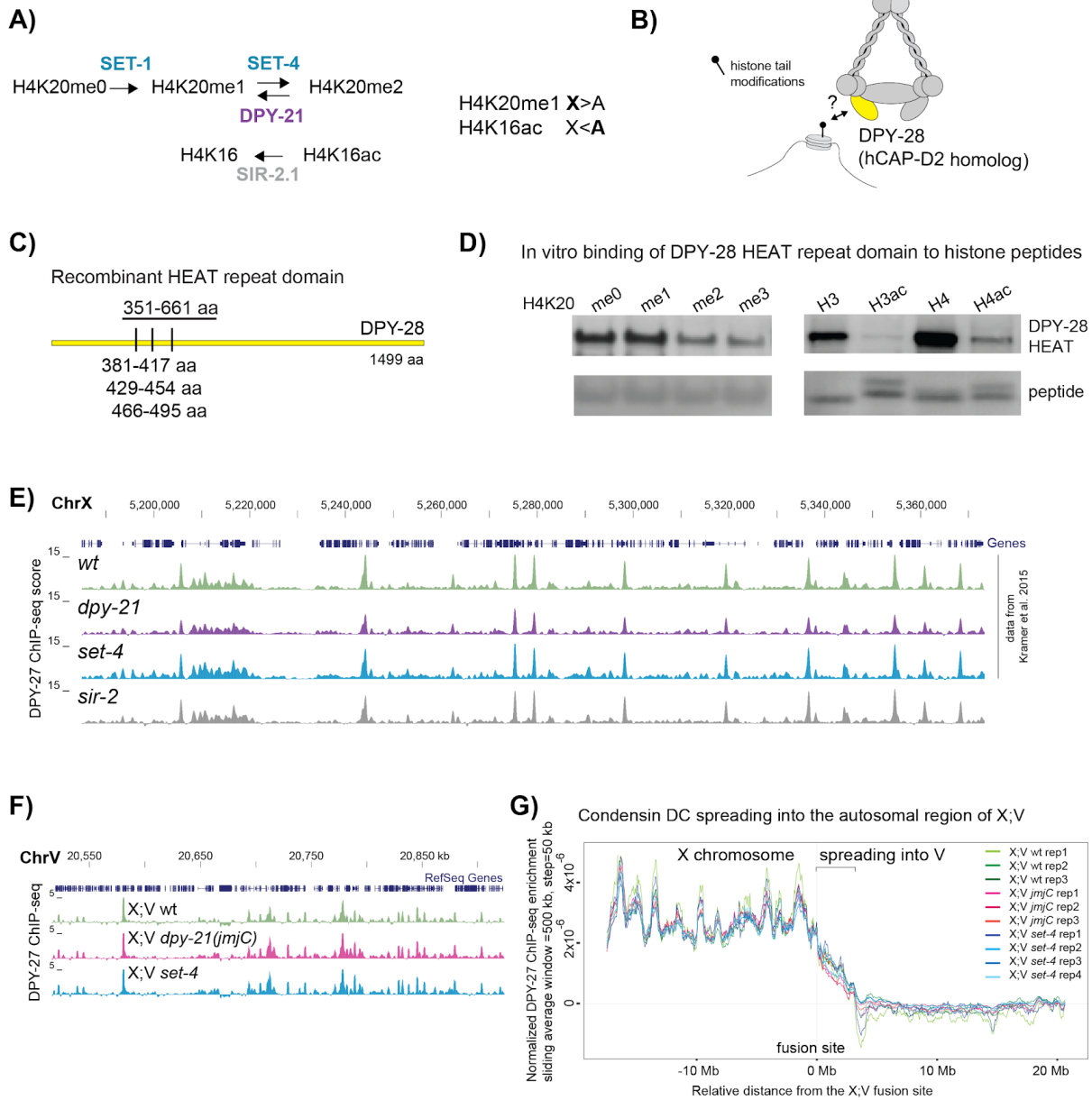**A)**

B)

C)

D)

E)

F)

G)

Figure 3) Condensin DC may interact with histone tails, but *set-4*, *sir-2.1*, and catalytic activity of *dpy-21* does not regulate condensin DC binding

> **A)** Enzymes that regulate H4K20 methylation and H4K16 acetylation. In hermaphrodites, H4K20me1 is increased, and H4K16ac is reduced on the dosage compensated X chromosomes compared to autosomes. *Dpy-21* null is *(e418)* allele with a premature stop codon that eliminates the protein [19], *Dpy-21(JmjC) is (y607)* allele, a

point mutation that nearly abolishes H4K20me2 demethylase activity without eliminating the protein itself [20]. *Set-4* null is *(n4600),* a knockout allele that eliminates H4K20me2/3 [60]. *Sir-2.1* null is *(ok434),* a knockout allele that increases H4K16ac [22].

B) Cartoon depicting possible interaction of HEAT repeat-containing domain of DPY-28 (homologous to human hCAPD-2) with histone tail modifications.

C) Three HEAT repeats annotated by pfam are shown as tick marks. The amino acids 351-661 were purified and used in peptide binding.

D) In solution peptide binding assay was performed using GST-tagged DPY-28 HEAT domain and biotinylated histone N-terminal tail peptides with indicated modifications. The recombinant protein was incubated with peptides bound to magnetic streptavidin beads, and bound fractions were analyzed using western blot. The streptavidin signal below indicates the amount of peptide in each fraction.

E) UCSC genome browser shot of a representative region showing similar DPY-27 ChIP-seq patterns in wild-type and *sir-2.1*. Data from wild-type N2, *dpy-21* null, *set-4* null are from [31] and are plotted for comparison.

F) Genome browser view of DPY-27 ChIP-seq enrichment across the fusion site on the autosomal region of the X;V chromosome in X;V wild-type, *dpy-21(JmjC)* and *set-4* null backgrounds.

G) A moving average of the DPY-27 ChIP enrichment score is plotted with a window size of 200 kb and step size of 20 kb in X;V fusion strains with wild-type, *dpy-21(JmjC),* and *set-4* null backgrounds. DPY-27 ChIP-seq data was normalized to reduce variability between replicates by z score standardization ChIP/Input ratios to the background from autosomes I-IV followed by equalization of total ChIP-seq signal to 1 in X:V.

Supplemental figure 3

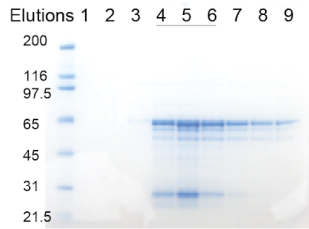**A)** Differential expression analysis mRNA-seq
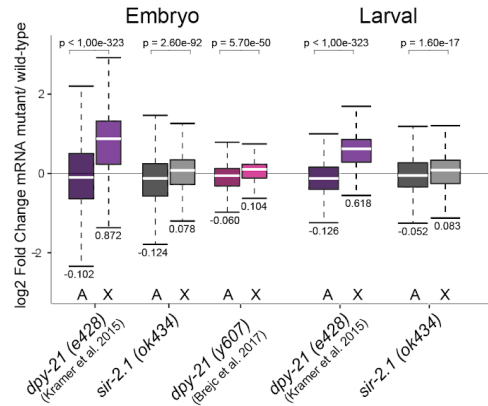
B) Dumpiness measurement
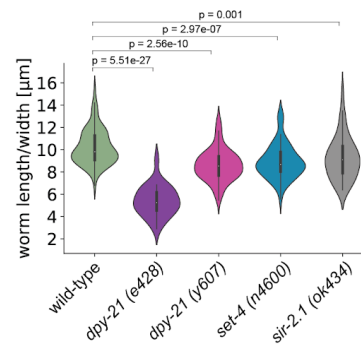
C) Purification of recombinant HEAT domain
351-661 aa
Pooled fractions: 4-6, 0.5 µg/µl, 60 kDa

D) Peptides used for in solution peptide pull down assay

|		Sequence
H3 unmodified	H3 1-20	AR²TK⁴QTAR⁶K⁹S¹⁰TGGK¹⁴APRK¹⁸QL-K(Biot)-NH₂
H3 tetra acetyl	H3 1-20	ARTK(Ac)QTARK(Ac)STGGK(Ac)APRK(Ac)QL-K(Biot)-NH₂
H4 unmodified	H4 1-23	Ac-SGRGK⁵GGKGLGKGGAKRHRKVLR-Peg-Biot
H4 tetra acetyl	H4 1-23	Ac-SGRGK(Ac)GGK(Ac)GLGK(Ac)GGAK(Ac)RHRKVLR-Peg-Biot
H4K20me0		SGRGKGGKGLGKGGAKRHRKVLR-Peg-Biot
H4K20me1		SGRGKGGKGLGKGGAKRHRK(Me)VLR-Peg-Biot
H4K20me2		SGRGKGGKGLGKGGAKRHRK(Me2)VLR-Peg-Biot
H4K20me3		SGRGKGGKGLGKGGAKRHRK(Me3)VLR-Peg-Biot

E)

F)
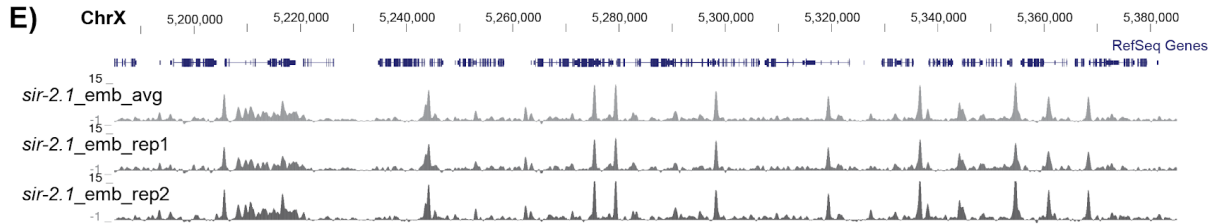
Figure 3) Supplements

A) mRNA-seq analysis comparing published *dpy-21 (e428)* from *[31]*, *dpy-21(JmjC)* data from [20], and new data in *sir-2.1* null mutant in embryos (left) and larvae (right). The level of X chromosome derepression compared to autosomes was compared in different mutants using log2 expression ratios compared to wild-type. Significant X chromosome upregulation was tested by a Wilcoxon–Mann–Whitney test. Median values of each group of genes are shown below each boxplot.

B) Dumpiness phenotype analysis of wild-type and different mutant worms. The length divided by the width of young adult worms was calculated as a proxy for their dumpiness level from two biological replicates. The following number of worms were used for each condition: wild-type: n= 102; *dpy-21(e428)*: n= 24; *dpy-21(y607)*: n= 67; *set-4 (n4600)*: n= 69; *sir-2.1(ok434)*: n= 51. P values are from an independent two-sample t-test.

C) Elutions of GST-DPY-28 HEAT repeat domain recombinant protein, predicted to be ~60 kDa. Fractions 4-6 were pooled for peptide binding assay.

D) Sequences and modifications of the N-terminal histone peptides analyzed.

E) UCSC genome browser shot of a representative region showing similar DPY-27 ChIP-seq patterns in wild-type and *sir-2.1* replicates.

F) UCSC genome browser shot of replicates corresponding to Figure 3F. Genome browser view of DPY-27 ChIP-seq enrichment on the X chromosomal region of the X;V chromosome in X;V wild-type, *dpy-21(JmjC)* and *set-4* null backgrounds.

DPY-21 has a non-catalytic activity that increases the mobile fraction of condensin DC

Since the histone modifiers showed little effect on condensin DC binding as measured by ChIP-seq, we used our established FRAP system in mutants and knockdown conditions to study these proteins' influence on condensin DC dynamics. In *set-1* knockdown, *set-4* null, *sir-2.1* null, and *dpy-21(JmjC)* mutants, DPY-27 FRAP recovery was similar to that of wild-type (Figure 4A,

Supplemental Figure 4A). Thus, *set-1*, *set-4*, *sir-2.1,* and the catalytic activity of *dpy-21* act downstream of condensin DC to contribute to X chromosome repression.

In contrast, the *dpy-21* null mutation caused a striking change in DPY-27::GFP recovery (Figure 4A). The *dpy-21* null mutant reduced the percentage of mobile DPY-27::GFP from ~30% to ~10% (Figure 4B). A control experiment bleaching DPY-27::GFP outside of the X indicated that the effect of the *dpy-21* null mutant is specific to the X (Supplemental Figure 4B). Thus, DPY-21 increases the proportion of mobile condensin DC molecules on the X chromosomes. Together, these results suggest that DPY-21 has two functions in X chromosome dosage compensation. One is catalytic and acts downstream of condensin DC to contribute to X chromosome repression. The second one is non-catalytic, acting upstream of condensin DC to regulate the dynamics of complex binding, which is important for X chromosome repression.

Previous analysis of condensin DC localization by immunofluorescence in the *dpy-21* null mutant had not reported an effect except an increase in the volume of the X chromosomes in *dpy-21* null and *JmjC* mutants [18,20]. We wondered if the reduction of mobile condensin DC produces a difference in the confocal imaging of DPY-27::Halo signal compared to wild type. Indeed, we noticed stronger puncta of DPY-27 signal within the X chromosomal domain in the *dpy-21* null mutant, which appears as a long tail of high pixel intensities in the distribution (Figure 4C, Supplemental Figure 4C).
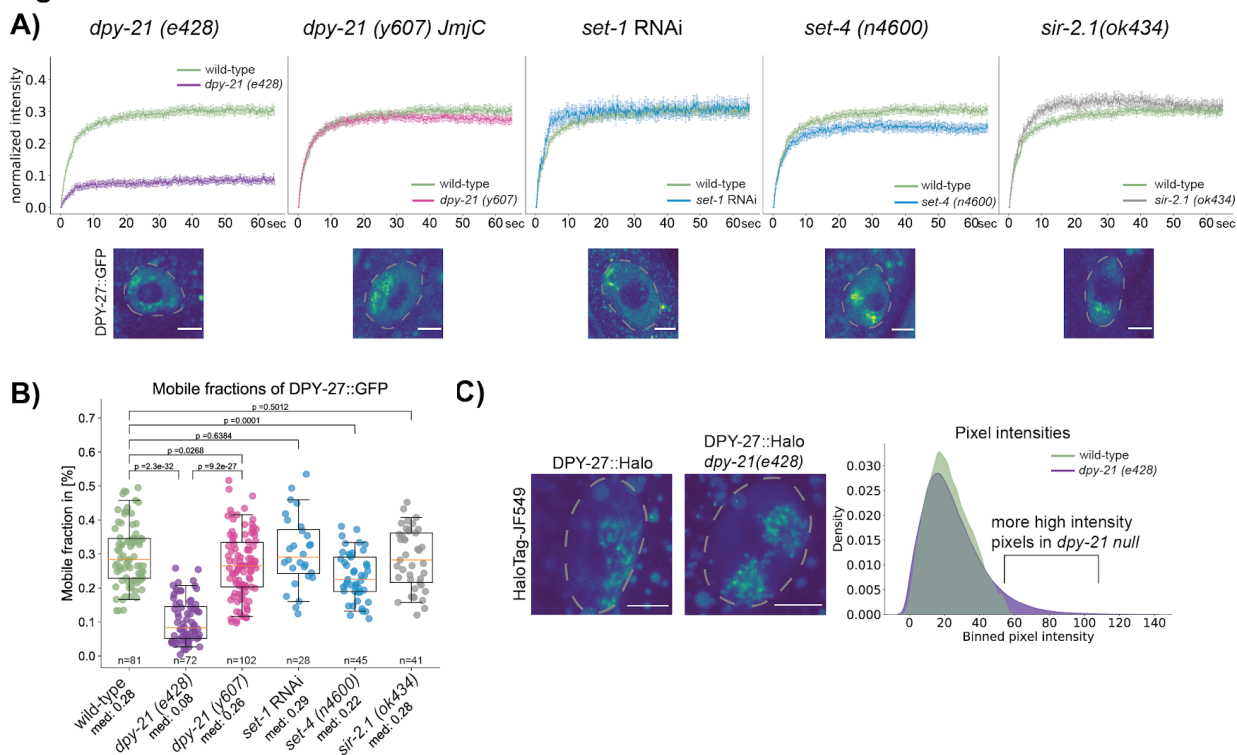
Figure 4

Figure 4 DPY-21 null but not catalytic mutant reduces the proportion of mobile condensin DC

A) Mean FRAP recovery curves of DPY-27::GFP in either wild-type (green) or different mutant conditions. Error bars denote s.e.m.. Number of bleached single intestine nuclei (from at least 3 biological replicates) for each experiment is n = 81 for wild-type, n = 72 for *dpy-21 (e428)*, n = 102 for *dpy-21 (y607), set-1 RNAi* n = 28, *set-4 (n4600)* n = 45, *sir-2.1 (ok434)* n= 41. Corresponding images of intestine nuclei for each mutant condition are depicted under each FRAP curve. Scale bar = 5 μm.

B) Mobile fractions calculated from individual replicate FRAP recovery curves in panel A. P values are from an independent two-sample t-test. The number of used images of nuclei is noted under each boxplot.

C) Analysis of endogenous DPY-27::Halo fluorescent intensity enrichment on the X chromosome compared in wild-type and *dpy-21* null worms. The HaloTag stained signal of DPY-27 was segmented and quantified in adult intestine cells in two biological replicates (Supplemental figure 3E). The left panel depicts two example nuclei (marked
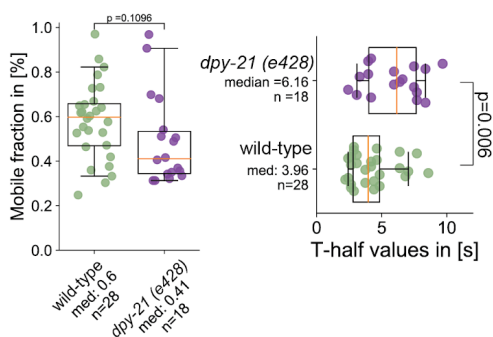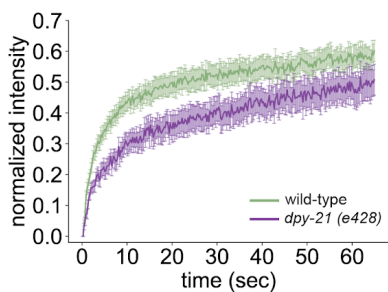
with a dotted line). Scale bar corresponds to 5 μm. For the wild-type worms, 17 images were analyzed, for the *dpy-21(e428)* mutant images of 31 nuclei were analyzed. The right panel shows the binned mean pixel fluorescence intensity for the two conditions.

Supplement figure 4

A) T-half values of DPY-27::GFP
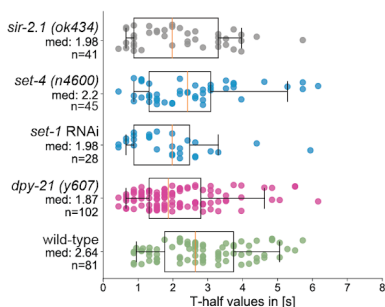
B)

FRAP recovery of background signal

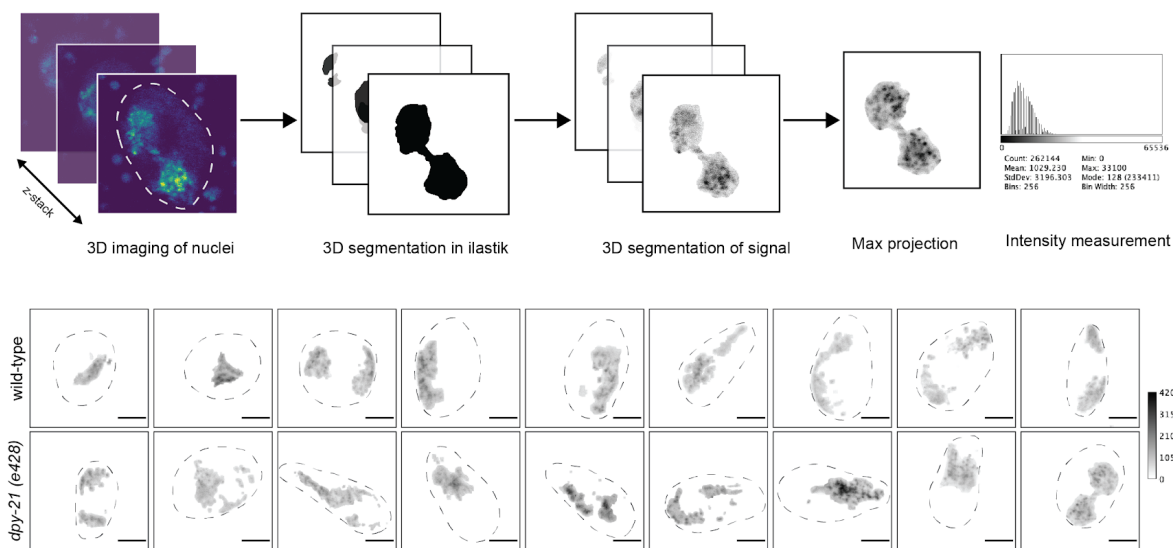**C)** Intensity measurement of DPY-27::Halo

Figure 4 Supplements

A) T-half recovery time calculated from individual replicate FRAP recovery curves in Figure 4A. The T-half value for *dpy-21 (e428)* is not included in the plot due to the very low recovery during the experimental time frame.

B) Mean FRAP recovery curves for background DPY-27::GFP in wild-type and *dpy-21 (e428)* mutant worms. FRAPs were performed 8 hours after a 1-hour heat-shock at 35°C. Unlike Figure 4A, the bleach point was not placed outside the X chromosomal area. Error bars for the bleach curves denote s.e.m. Number of bleached single intestine nuclei (from 2 biological replicates) for each experiment is n = 28 for wild-type and n = 18 for *dpy-21 (e428)*. The middle panel depicts the mobile fractions for the background recovery. The right panel depicts the T-half recovery times for the background recovery. P values are from an independent two-sample t-test.

C) Analysis of the fluorescence intensity of endogenously tagged DPY-27::Halo, for wild-type and *dpy-21 (e428)* worms. The top row shows the analysis pipeline for the 3D segmentation of the HaloTag-JF549 signal. Z-stacks of intestine nuclei were imaged and segmented in 3D using ilastik [45]. The resulting mask was used to segment the fluorescent signal in 3D, and from max projections, binned intensities were obtained. The bottom row depicts example images of 3D segmented and max projected nuclei of the wild-type and mutant worms. The scale bar corresponds to 5 µm, and all images are calibrated to the same gray values.

3D DNA contacts as measured by Hi-C does not change significantly in the *dpy-21* null

Since *dpy-21* null mutation decreased the number of mobile condensin DC molecules as measured by FRAP, we reasoned that DPY-21 might act similar to the cohesin unloader WAPL [61]. To test this idea, we performed Hi-C analysis in *dpy-21* null embryos and in parallel analyzed published Hi-C data in the catalytic mutant *dpy-21(JmjC(y607))* [20]. While a subtle reduction in insulation was observed across a few *rex* sites that act as TAD boundaries, the overall TAD structure of the X was similar to that of the corresponding wild-type in *dpy-21* null embryos (Figure 5A). Furthermore, the range of DNA interactions in the *dpy-21* null mutant was

more similar to the wild-type compared to *dpy-21(JmjC)* on the X chromosomes (Figure 5B) and autosomes (Supplemental Figure 5A) [20].

To highlight condensin DC-mediated X-specific 3D contacts, we normalized contact frequency across the same distance on the X to autosomes. This analysis reaffirmed that compared to autosomes, DNA contacts between 50 kb to 1 Mb range (approximated based on X/A > 1) are more frequent on the X (Figure 5C). The *dpy-21* null mutant does not show the shift towards shorter X-enriched DNA contacts seen in *dpy-21(JmjC)* (Supplemental Figure 5B). Similarly, the long-range interactions between *rex* sites are less reduced in the null compared to the *JmjC* mutant (Figure 5D). Thus, we conclude that changes in X-enriched DNA contacts due to decreased H4K20me1 in the *JmjC* mutant are partially offset by the loss of the DPY-21 protein.
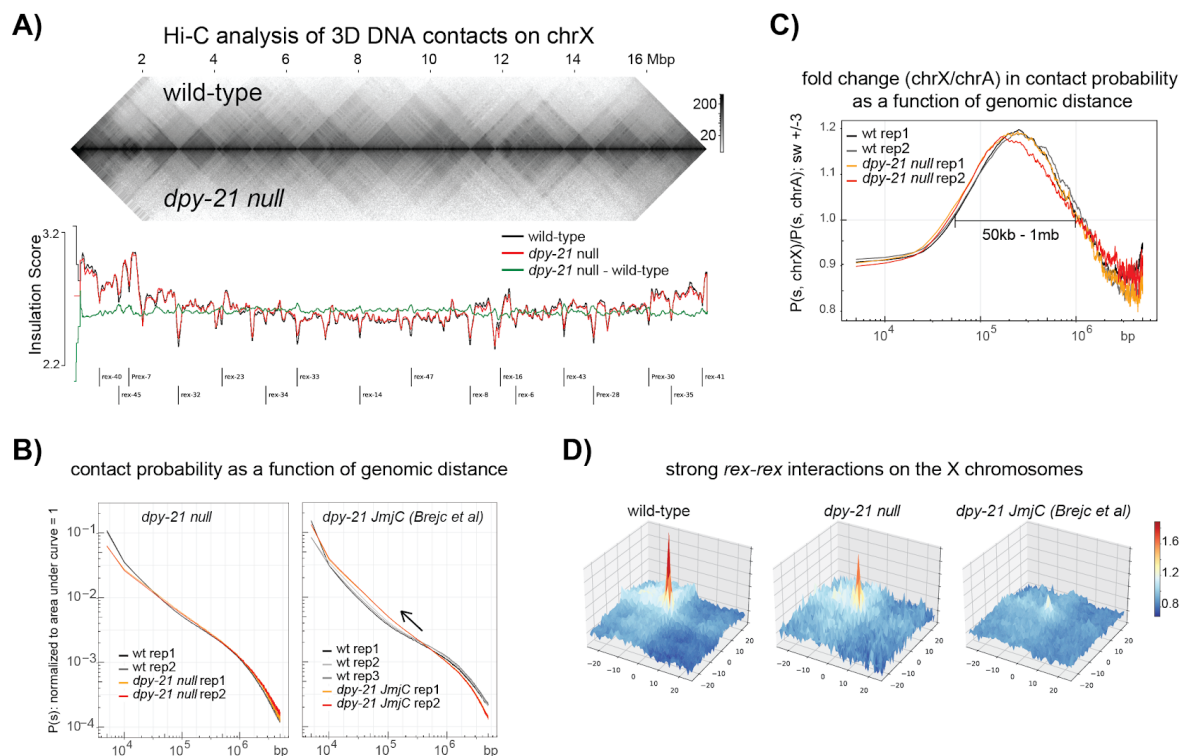
Figure 5

A) Hi-C analysis of 3D DNA contacts on chrX

B) contact probability as a function of genomic distance

C) fold change (chrX/chrA) in contact probability as a function of genomic distance

D) strong *rex-rex* interactions on the X chromosomes

Figure 5) Hi-C analysis of 3D DNA contacts in the *dpy-21* null mutant embryos

A) Hi-C heatmap and insulation scores of chromosome-X showing wild-type and the *dpy-21* null mutant. The insulation scores for wild-type, mutant, and mutant minus wild-type are shown below with the annotated strong *rex* sites.

B) For the X chromosomes, distance decay curve showing the relationship between 5 kb binned genomic separation, s, and average contact probability, P(s). Each plot is normalized to unity. *JmjC* mutant data was downloaded from and analyzed with the same parameters as the *dpy-21* null, using corresponding wild-type data [20].

C) X-A normalized distance decay curve for *dpy21* null. For every genomic separation s, the unity normalized contact probability of X-chromosome, P(s,chrX), is divided by that of autosomes, P(s,chrA). A moving average of +/- 3 bins is applied for plotting.

D) Meta-'dot' plot showing the average strength of interactions between pairs of *rex* sites on a distance-normalized matrix. For 17 strong *rex* sites, a total of 33 *rex-rex* pairs located within 3 Mb of each other were used.
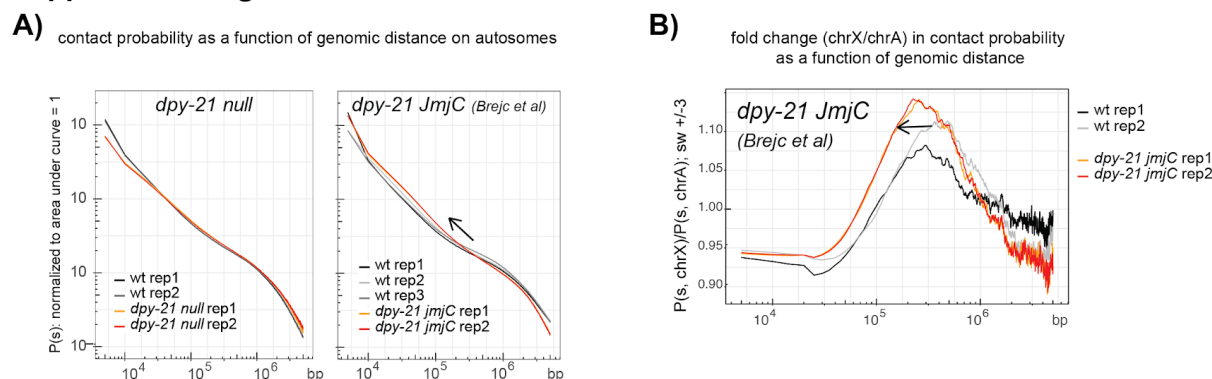
Supplemental Figure 5

A) contact probability as a function of genomic distance on autosomes

B) fold change (chrX/chrA) in contact probability as a function of genomic distance

Figure 5) Supplement

A) For the autosomes, a distance decay curve showing the relationship between 5 kb binned genomic separation, s, and average contact probability, P(s). Each plot is normalized to unity. *JmjC* mutant data was downloaded from and analyzed with the same parameters as the *dpy-21* null, using corresponding wild-type data [20].

B) X-A normalized distance decay curve for *JmjC* mutant. For every genomic separation s, the unity normalized contact probability of X-chromosome, P(s,chrX), is divided by that of Autosomes, P(s,chrA). A moving average of +/- 3 bins is applied for plotting. Wild-type replicate three from [20] was an outlier and excluded from the analysis.

DISCUSSION

In vivo and *in vitro* studies show that SMC complex function requires ATPase activity [1,62]. In *C. elegans* condensin DC, four out of five subunits also function within the condensin I complex, thus their functional homology is apparent [8]. The single subunit that distinguishes condensin DC from condensin I is DPY-27, the SMC4 homolog [8,63]. Here we showed that a single amino acid mutation that has been shown to slow down ATP hydrolysis and impair the function of SMC4 proteins in other organisms also eliminates DPY-27 binding (Figure 2). This observation adds to evidence that the evolutionarily conserved SMC complex activity is conserved in condensin DC [7,64,65].

What is the role of ATPase activity in SMC complex binding to DNA?

DPY-27 EQ mutation eliminating its binding measured by ChIP-seq and FRAP suggests that stable association of condensin DC with the X chromosomes requires ATP hydrolysis (Figure 2). Although ATPase activity is strictly conserved, there may be differences in how different SMC complexes and organisms are affected by ATPase mutations. In *Xenopus* extracts, incorporating the EQ mutation in SMC-2 and SMC-4 did not abolish loading to chromosomes analyzed by immunofluorescence (IF) [53]. Similar results were obtained in chicken cell culture and yeast where SMC-2 and SMC-4 EQ single mutants were able to bind chromosomes at levels comparable to the WT but were not competent in chromosome compaction [46,55]. In *Bacillus subtilis,* ChIP-seq experiments showed that the EQ mutant SMC bound to *parS* loading sites but had reduced spreading along the chromosome [66]. Similarly, mammalian EQ mutant cohesin

binding at loading sites was less affected than at CTCF sites [52]. Thus different modes of binding may have different ATPase requirements.

Is ATPase activity required for the formation and stability of SMC complexes?

ATPase activity may also contribute to SMC complex formation and stability *in vivo*, perhaps by controlling the structural changes that occur through the cycle of ATP binding and hydrolysis [67]. While in chicken, no measurable effect of ATPase mutation was reported for complex formation measured by pull-down experiments [55], in budding yeast, ATP binding mutation reduced the interaction between SMC-4 and the kleisin subunit [46], and in *B. subtilis*, ATPase mutations reduced the SMC homodimer's proper interaction with the ScpA bridging protein as measured by crosslinking assay [68]. We have also noticed reduced co-IP interaction with the kleisin subunit by DPY-27(EQ), which resulted in degradation of the protein over time (Figure 2B). A similar reduction in SMC2/4 ATPase mutant protein levels was reported in budding yeast [46]. These observations suggest that the ATPase cycle affects the formation and stability of condensins *in vivo*.

How do chromatin and histone modifications affect condensin binding in vivo?

The potential for HEAT repeat domains in CAP-D3 and CAP-G2 to interact with histones was put forward for human condensin II [58]. Here, we found that the recombinant HEAT repeat domain of DPY-28 interacts with histone H3 and H4 tail peptides in a manner sensitive to the modifications tested (Figure 3). Yet, mutants that reduce X-enrichment of H4K20me1 and increase X-depletion of H4K16ac did not affect condensin DC binding as measured by ChIP-seq and FRAP (Figure 3, 4). Thus, H4K20me1 and H4K16ac act downstream of condensin DC to repress transcription.

In vitro, condensin prefers binding to free DNA [59,69,70], and *in vivo* ChIP-seq analysis of condensins in various organisms revealed that condensins are accumulated at accessible regions of the genome [71,72]. Interestingly, a recent study found that condensin is able to extrude DNA fragments containing 3-4 nucleosomes, and the nucleosomes increased the velocity and

processivity of condensin II *in vitro* [70]. Thus, nucleosomes may regulate the ATPase-dependent movement of condensin *in vivo*. In addition to nucleosomes themselves, chromatin modifications, histone variants, and linker histone were proposed to regulate condensin binding [58,73–79]. It remains unclear if the combined effects of multiple histone modifications, variants, and linker histones on the X chromosomes regulate condensin DC binding.

How does DPY-21 function in X chromosome dosage compensation?

DPY-21 is an H4K20me2 demethylase that interacts with condensin DC and is important for dosage compensation [19,20]. Comparison of the null and catalytic mutants indicated that DPY-21 plays both a structural and catalytic role in X chromosome repression [20]. The catalytic role of *dpy-21* is downstream of condensin DC binding and contributes to X chromosome repression. Here, we showed that DPY-21 has a non-catalytic role upstream of condensin DC, increasing the mobile fraction of the complex on the X chromosomes, which is critical for transcription repression.

How does DPY-21 increase the proportion of the mobile condensin DC complexes? We reasoned that if DPY-21 removes condensin DC from chromatin, it could be akin to the cohesin unloader, where Hi-C analysis in WAPL mutant showed enrichment of longer-range cohesin-mediated 3D contacts [61,80]. In the *JmjC* catalytic mutant, long-range interactions between *rex* sites were diminished [20]. Further elimination of non-catalytic DPY-21 activity in the *dpy-21* null mutant rescued the X-enriched long-range interactions, including between *rex* sites, suggesting that the non-catalytic function of DPY-21 may be to unload condensin DC. In the absence of knowing how histone modifications themselves affect 3D DNA contacts and the structural connection between DPY-21 and condensin DC, it is difficult to address how one protein, DPY-21 has two opposing activities on 3D DNA contacts. Since *dpy-21(JmjC)* does not regulate condensin DC binding, we speculate that DPY-21 catalytic activity regulates the properties of chromatin fiber to promote long-range 3D interactions. The non-catalytic activity may reduce condensin DC

residence on chromatin, thus decreasing the range of 3D interactions. Put together, these two opposing activities largely cancel each other.

In summary, here we found that a non-catalytic function of DPY-21 is to increase the mobile fraction of condensin DC. Interestingly, while X chromosomes are depressed ~2-fold in the *dpy-21* null mutant, there is little change in the X-enriched 3D DNA contacts measured by Hi-C. We speculate that the basis of this discrepancy lies in Hi-C detecting changes between the equilibrium states. It is possible that for condensin-DC mediated transcription repression, the process of binding and generating loops is more important than the size or the total number of loops that are introduced. Therefore, we conclude that DPY-21 regulates the dynamics of condensin DC binding to chromatin, which is important for its function in transcription repression (Figure 6).
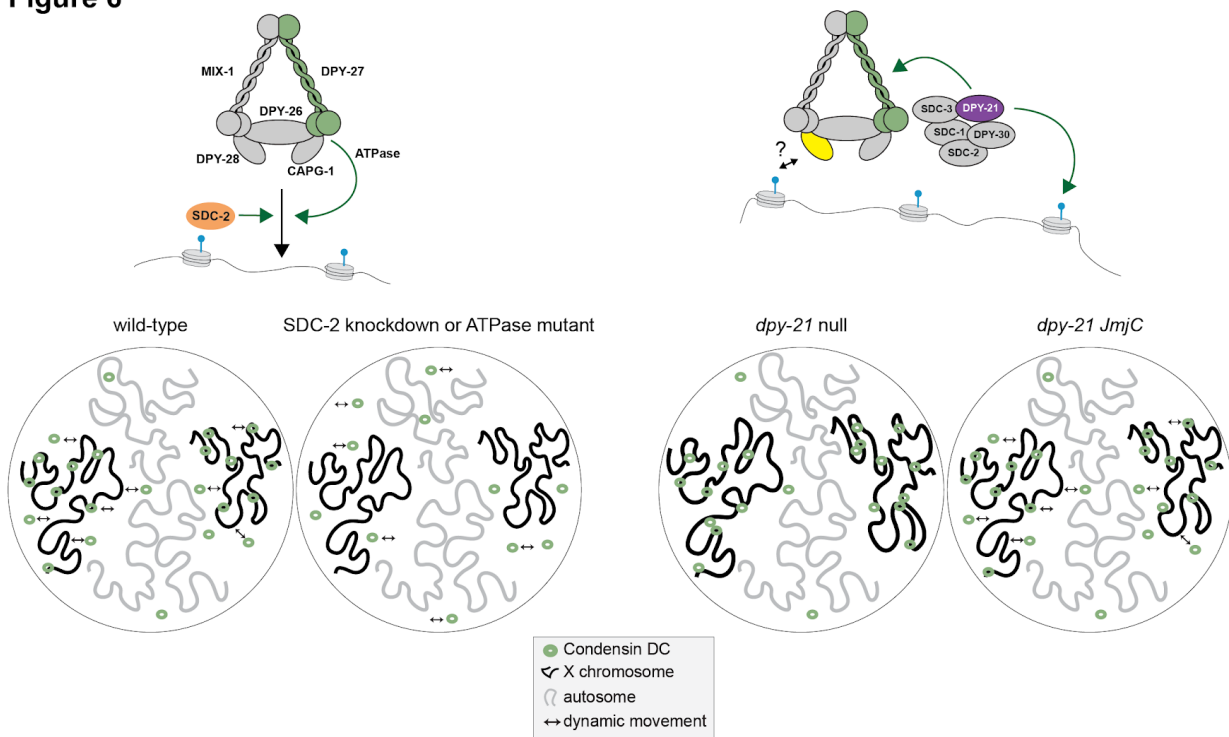
Figure 6

Figure 6) Model for regulation of condensin DC binding

In a wild-type hermaphrodite cell, condensin DC binds dynamically to the X chromosomes. This binding is disrupted by a knockdown of its recruiter SDC-2 or a single amino acid mutation in the ATPase domain of DPY-27. Condensin DC may interact with histone tails through HEAT-repeats within DPY-28. H4K20me2 demethylase, DPY-21 has a dual function in X chromosome repression. The catalytic activity increases H4K20me1 on the X and contributes to repression downstream of condensin DC. The non-catalytic activity of DPY-21 is to increase the turnover of condensin DC molecules, which is important for transcription repression. In the *dpy-21* null condition, both catalytic and non-catalytic activities are eliminated, resulting in stronger X chromosome derepression.

References

1 Hirano, T. (2016) Condensin-Based Chromosome Organization from Bacteria to Vertebrates. *Cell* 164, 847–857

2 Paul, M.R. *et al.* (2018) Condensin Depletion Causes Genome Decompaction Without

Altering the Level of Global Gene Expression in Saccharomyces cerevisiae. *Genetics* 210, genetics.301217.2018

3 Goloborodko, A. et al. (2016) Chromosome Compaction by Active Loop Extrusion. *Biophysical journal* 110, 2162–2168

4 Cacciatore, Á.S. and Rowland, B.D. (2019) Loop formation by SMC complexes: turning heads, bending elbows, and fixed anchors. *Current opinion in genetics & development* 55, 11–18

5 Paul, M.R. et al. (2018) Condensin action and compaction. *Curr Genet* 65, 407–415

6 Meyer, B.J. (2005) X-Chromosome dosage compensation. *WormBook* DOI: 10.1895/wormbook.1.8.1

7 Albritton, S.E. and Ercan, S. (2018) Caenorhabditis elegans Dosage Compensation: Insights into Condensin- Mediated Gene Regulation. *Trends in Genetics* 34, 41–53

8 Csankovszki, G. et al. (2009) Three Distinct Condensin Complexes Control C. elegans Chromosome Dynamics. *Curr Biol* 19, 9–19

9 Csankovszki, G. et al. (2004) Recruitment and spreading of the C. elegans dosage compensation complex along X chromosomes. *Science* 303, 1182–1185

10 Jans, J. et al. (2009) A condensin-like dosage compensation complex acts at a distance to control expression throughout the genome. *Genes & Development* 23, 602–618

11 Albritton, S.E. et al. (2017) Cooperation between a hierarchical set of recruitment sites targets the X chromosome for dosage compensation. *eLife* 6, e23645-29

12 Ercan, S. et al. (2009) The C. elegans Dosage Compensation Complex Propagates Dynamically and Independently of X Chromosome Sequence. *Current Biology* 19, 1777–1787

13 Street, L.A. et al. (2019) Binding of an X-Specific Condensin Correlates with a Reduction in Active Histone Modifications at Gene Regulatory Elements. Genetics 212, 729–742

14 Jimenez, D.S. et al. (2021) Condensin DC spreads linearly and bidirectionally from recruitment sites to create loop-anchored TADs in C. elegans. DOI: 10.1101/2021.03.23.436694

15 Rowley, M.J. et al. (2020) Analysis of Hi-C data using SIP effectively identifies loops in organisms from C. elegans to mammals. *Genome Res* 30, 447–458

16 Crane, E. et al. (2015) Condensin-driven remodelling of X chromosome topology during dosage compensation. *Nature* 523, 240–244

17 Anderson, E.C. et al. (2019) X Chromosome Domain Architecture Regulates Caenorhabditis elegans Lifespan but Not Dosage Compensation. *Developmental Cell* 51, 192-207.e6

18 Lau, A.C. et al. (2014) The C. elegans dosage compensation complex mediates interphase X chromosome compaction. *Epigenetics & chromatin* 7, 31–16

19 Yonker, S.A. and Meyer, B.J. (2003) Recruitment of C. elegans dosage compensation proteins for gene-specific versus chromosome-wide repression. Development 130, 6519–6532

20 Brejc, K. et al. (2017) Dynamic Control of X Chromosome Conformation and Repression by a Histone H4K20 Demethylase. Cell 171, 85-102.e23

21 Vielle, A. et al. (2012) H4K20me1 contributes to downregulation of X-linked genes for C. elegans dosage compensation. *PLoS genetics* 8, e1002933

22 Wells, M.B. et al. (2012) Caenorhabditis elegans Dosage Compensation Regulates Histone H4 Chromatin State on X Chromosomes. *Mol Cell Biol* 32, 1710–1719

23 Schmitz, M.L. et al. (2020) Priming chromatin for segregation: functional roles of mitotic histone modifications. *Cell Cycle* 19, 625–641

24 Frøkjær-Jensen, C. et al. (2008) Single-copy insertion of transgenes in Caenorhabditis elegans. *Nature Genetics* 40, 1375–1383

25 Dokshin, G.A. et al. (2018) Robust Genome Editing with Short Single-Stranded and Long, Partially Single-Stranded DNA Donors in Caenorhabditis elegans. Genetics 210, 781–787

26 Ercan, S. et al. (2007) X chromosome repression by localization of the C. elegans dosage compensation machinery to sites of transcription initiation. Nature Genetics 39, 403–408

27 Langmead, B. and Salzberg, S.L. (2012) Fast gapped-read alignment with Bowtie 2. *Nat Methods* 9, 357–359

28 Ramirez-Gonzalez, R.H. et al. (2012) Bio-samtools: Ruby bindings for SAMtools, a library for accessing BAM files containing high-throughput sequence alignments. *Source Code Biology Medicine* 7, 6

29 Ramírez, F. et al. (2016) deepTools2: a next generation web server for deep-sequencing data analysis. *Nucleic Acids Res* 44, W160–W165

30 Ho, J.W.K. et al. (2014) Comparative analysis of metazoan chromatin organization. Nature 512, 449–452

31 Kramer, M. et al. (2015) Developmental Dynamics of X-Chromosome Dosage Compensation by the DCC and H4K20me1 in C. elegans. PLoS genetics 11, e1005698

32 Kim, D. et al. (2013) TopHat2: accurate alignment of transcriptomes in the presence of insertions, deletions and gene fusions. *Genome Biol* 14, R36

33 Anders, S. et al. (2015) HTSeq—a Python framework to work with high-throughput sequencing data. *Bioinformatics* 31, 166–169

34 Love, M.I. et al. (2014) Moderated estimation of fold change and dispersion for RNA-seq data with DESeq2. Genome Biol 15, 550

35 Durand, N.C. et al. (2016) Juicer Provides a One-Click System for Analyzing Loop-Resolution Hi-C Experiments. *Cell Syst* 3, 95–98

36 Wolff, J. et al. (2018) Galaxy HiCExplorer: a web server for reproducible Hi-C data analysis, quality control and visualization. Nucleic Acids Res 46, gky504-

37 Ramírez, F. et al. (2018) High-resolution TADs reveal DNA sequences underlying genome organization in flies. *Nat Commun* 9, 189

38 Wolff, J. et al. (2020) Galaxy HiCExplorer 3: a web server for reproducible Hi-C, capture Hi-C and single-cell Hi-C data analysis, quality control and visualization. Nucleic Acids Res 48, W177–W184

39 Schindelin, J. et al. (2012) Fiji: an open-source platform for biological-image analysis. *Nature Methods* 9, 676–682

40 Moore, B.T. et al. (2013) WormSizer: High-throughput Analysis of Nematode Size and

Shape. *Plos One* 8, e57142

41 Grimm, J.B. et al. (2015) A general method to improve fluorophores for live-cell and single-molecule microscopy. Nature Methods 12, 244–250

42 Grimm, J.B. et al. (2017) A general method to fine-tune fluorophores for live-cell and in vivo imaging. Nature Methods 14, 987–994

43 Wu, Y. et al. (2019) Single-molecule dynamics of the P granule scaffold MEG-3 in the Caenorhabditis elegans zygote. *Molecular biology of the cell* 30, 333–345

44 Guizar-Sicairos, M. et al. (2008) Efficient subpixel image registration algorithms. *Opt Lett* 33, 156

45 Berg, S. et al. (2019) ilastik: interactive machine learning for (bio)image analysis. Nat Methods 16, 1226–1232

46 Thadani, R. et al. (2018) Cell-Cycle Regulation of Dynamic Chromosome Association of the Condensin Complex. *Cell Reports* 23, 2308–2317

47 Gerlich, D. et al. (2006) Condensin I Stabilizes Chromosomes Mechanically through a Dynamic Interaction in Live Cells. Current Biology 16, 333–344

48 Walther, N. et al. (2018) A quantitative map of human Condensins provides new insights into mitotic chromosome architecture. *J Cell Biology* 217, 2309–2328

49 Mueller, F. et al. (2013) Quantifying transcription factor kinetics: At work or at play? *Crit Rev Biochem Mol* 48, 492–514

50 Kimura, H. and Cook, P.R. (2001) Kinetics of Core Histones in Living Human CellsLittle Exchange of H3 and H4 and Some Rapid Exchange of H2b. J Cell Biology 153, 1341–1354

51 Mazza, D. et al. (2012) A benchmark for chromatin binding measurements in live cells. Nucleic Acids Res 40, e119–e119

52 Vian, L. et al. (2018) The Energetics and Physiological Impact of Cohesin Extrusion. Cell 173, 1165-1178.e20

53 Kinoshita, K. et al. (2015) Balancing acts of two HEAT subunits of condensin I support dynamic assembly of chromosome axes. Developmental Cell 33, 94–106

54 Hirano, M. and Hirano, T. (2004) Positive and negative regulation of SMC-DNA interactions by ATP and accessory proteins. *Embo Journal* 23, 2664–2673

55 Hudson, D.F. et al. (2008) Molecular and genetic analysis of condensin function in vertebrate cells. Molecular biology of the cell 19, 3070–3079

56 Chao, L.F.-I. et al. (2017) An SMC-like protein binds and regulates Caenorhabditis elegans condensins. PLoS genetics 13, e1006614

57 Yoshimura, S.H. and Hirano, T. (2016) HEAT repeats - versatile arrays of amphiphilic helices working in crowded environments? *Journal of cell science* 129, 3963–3970

58 Liu, W. et al. (2010) PHF8 mediates histone H4 lysine 20 demethylation events involved in cell cycle progression. Nature DOI: 10.1038/nature09272

59 Kschonsak, M. et al. (2017) Structural Basis for a Safety-Belt Mechanism That Anchors Condensin to Chromosomes. Cell DOI: 10.1016/j.cell.2017.09.008

60 Delaney, C.E. et al. (2017) A histone H4 lysine 20 methyltransferase couples environmental cues to sensory neuron control of developmental plasticity. Development 144, dev.145722

61 Haarhuis, J.H.I. et al. (2017) The Cohesin Release Factor WAPL Restricts Chromatin Loop Extension. Cell 169, 693-700.e14

62 Hassler, M. et al. (2018) Towards a Unified Model of SMC Complex Function. *Current biology : CB* 28, R1266–R1281

63 Hagstrom, K.A. et al. (2002) C. elegans condensin promotes mitotic chromosome architecture, centromere organization, and sister chromatid segregation during mitosis and meiosis. Genes & Development 16, 729–742

64 Wood, A.J. et al. (2010) Condensin and cohesin complexity: the expanding repertoire of functions. *Nature Publishing Group* 11, 391–404

65 Lau, A.C. and Csankovszki, G. (2014) Condensin-mediated chromosome organization and gene regulation. *Frontiers in genetics* 5, 473

66 Minnen, A. et al. (2016) Control of Smc Coiled Coil Architecture by the ATPase Heads Facilitates Targeting to Chromosomal ParB/parS and Release onto Flanking DNA. Cell Reports 14, 2003–2016

67 Lee, B.-G. et al. (2020) Cryo-EM structures of holo condensin reveal a subunit flip-flop mechanism. *Nature structural & molecular biology* DOI: 10.1038/s41594-020-0457-x

68 Wilhelm, L. et al. (2015) SMC condensin entraps chromosomal DNA by an ATP hydrolysis dependent loading mechanism in Bacillus subtilis. eLife 4,

69 Piazza, I. et al. (2014) Association of condensin with chromosomes depends on DNA binding by its HEAT-repeat subunits. Nature Publishing Group DOI: 10.1038/nsmb.2831

70 Kong, M. et al. (2020) Human Condensin I and II Drive Extensive ATP-Dependent Compaction of Nucleosome-Bound DNA. Mol Cell 79, 99-114.e9

71 Jeppsson, K. et al. (2014) The Chromosomal Association of the Smc5/6 Complex Depends on Cohesion and Predicts the Level of Sister Chromatid Entanglement. *Plos Genet* 10, e1004680

72 Uhlmann, F. (2016) SMC complexes: from DNA to chromosomes. *Nature Reviews Molecular Cell Biology* DOI: 10.1038/nrm.2016.30

73 Kimura, K. and Hirano, T. (2000) Dual roles of the 11S regulatory subcomplex in condensin functions. *Proc National Acad Sci* 97, 11972–11977

74 Kim, H.-S. et al. (2009) An acetylated form of histone H2A.Z regulates chromosome architecture in Schizosaccharomyces pombe. *Nat Struct Mol Biol* 16, 1286–1293

75 Tada, K. et al. (2011) Condensin association with histone H2A shapes mitotic chromosomes. Nature DOI: 10.1038/nature10179

76 Tanaka, A. et al. (2012) Epigenetic Regulation of Condensin-Mediated Genome Organization during the Cell Cycle and upon DNA Damage through Histone H3 Lysine 56 Acetylation. Mol Cell 48, 532–546

77 Yuen, K.C. et al. (2017) Condensin II is anchored by TFIIIC and H3K4me3 in the mammalian genome and supports the expression of active dense gene clusters. *Science Advances*

3, e1700191

78 Petty, E.L. et al. (2009) Restricting Dosage Compensation Complex Binding to the X Chromosomes by H2A.Z/HTZ-1. Plos Genet 5, e1000699

79 Choppakatla, P. et al. (2020) Linker histone H1.8 inhibits chromatin-binding of condensins and DNA topoisomerase II to tune chromosome compaction and individualization. *Biorxiv* DOI: 10.1101/2020.12.20.423657

80 Nuebler, J. et al. (2018) Chromatin organization by an interplay of loop extrusion and compartmental segregation. Proc National Acad Sci 115, 201717730